

Mass-change And Geosciences International Constellation (MAGIC) expected impact on science and applications

I. Daras¹, G. March², R. Pail³, C. W. Hughes^{4,5}, C. Braitenberg⁶, A. Güntner^{7,8}, A. Eicker⁹, B. Wouters¹⁰, B. Heller-Kaikov³, T. Pivetta⁶ and A. Pastorutti⁶

¹European Space Agency, Earth & Mission Science Division, ESTEC, 2201 AZ Noordwijk, The Netherlands. E-mail: ilias.daras@esa.int

²RHEA for European Space Agency, Earth & Mission Science Division, ESTEC, 2201 AZ Noordwijk, The Netherlands

³Institute of Astronomical and Physical Geodesy, Technical University of Munich (TUM), Arcisstraße 21, D-80333 München, Germany

⁴School of Environmental Sciences, University of Liverpool, L3 5DA Liverpool, UK

⁵National Oceanography Centre, L3 5DA Liverpool, UK

⁶Department of Mathematics and Geosciences, University of Trieste, Via Weiss 1, I-34128 Trieste, Italy

⁷Helmholtz Centre Potsdam, GFZ German Research Centre for Geosciences, 14476 Potsdam, Germany

⁸Institute of Environmental Sciences and Geography, University of Potsdam, 14473 Potsdam, Germany

⁹HafenCity University Hamburg, 20457 Hamburg, Germany

¹⁰Department of Geoscience and Remote Sensing, Delft University of Technology, 2628 CN Delft, The Netherlands

Accepted 2023 December 4. Received 2023 December 3; in original form 2023 April 18

SUMMARY

The joint ESA/NASA Mass-change And Geosciences International Constellation (MAGIC) has the objective to extend time-series from previous gravity missions, including an improvement of accuracy and spatio-temporal resolution. The long-term monitoring of Earth's gravity field carries information on mass change induced by water cycle, climate change and mass transport processes between atmosphere, cryosphere, oceans and solid Earth. MAGIC will be composed of two satellite pairs flying in different orbit planes. The NASA/DLR-led first pair (P1) is expected to be in a near-polar orbit around 500 km of altitude; while the second ESA-led pair (P2) is expected to be in an inclined orbit of 65° – 70° at approximately 400 km altitude. The ESA-led pair P2 Next Generation Gravity Mission shall be launched after P1 in a staggered manner to form the MAGIC constellation. The addition of an inclined pair shall lead to reduction of temporal aliasing effects and consequently of reliance on de-aliasing models and post-processing. The main novelty of the MAGIC constellation is the delivery of mass-change products at higher spatial resolution, temporal (i.e. subweekly) resolution, shorter latency and higher accuracy than the Gravity Recovery and Climate Experiment (GRACE) and Gravity Recovery and Climate Experiment Follow-On (GRACE-FO). This will pave the way to new science applications and operational services. In this paper, an overview of various fields of science and service applications for hydrology, cryosphere, oceanography, solid Earth, climate change and geodesy is provided. These thematic fields and newly enabled applications and services were analysed in the frame of the initial ESA Science Support activities for MAGIC. The analyses of MAGIC scenarios for different application areas in the field of geosciences confirmed that the double-pair configuration will significantly enlarge the number of observable mass-change phenomena by resolving smaller spatial scales with an uncertainty that satisfies evolved user requirements expressed by international bodies such as IUGG. The required uncertainty levels of dedicated thematic fields met by MAGIC unfiltered Level-2 products will benefit hydrological applications by recovering more than 90 per cent of the major river basins worldwide at 260 km spatial resolution, cryosphere applications by enabling mass change signal separation in the interior of Greenland from those in the coastal zones and by resolving small-scale mass variability in challenging regions such as the Antarctic Peninsula, oceanography applications by monitoring meridional overturning circulation changes on timescales of years and decades, climate applications by detecting amplitude and phase changes of Terrestrial Water Storage after 30 yr in 64 and 56 per cent of the global land areas

and solid Earth applications by lowering the Earthquake detection threshold from magnitude 8.8 to magnitude 7.4 with spatial resolution increased to 333 km.

Key words: Global change from geodesy; Satellite gravity; Time variable gravity; Glaciology; Hydrology; Earthquake dynamics.

1 INTRODUCTION

Continuity and evolution of gravity missions to observe mass change is foreseen around the turn of this decade in order to meet priority user needs not addressed by the existing and planned satellite infrastructure. The global scientific user community has been continuously addressing the need for enhanced and sustained mass-change monitoring from space, via bodies such as the Global Geodetic Observing System, International Association of Geodesy and the International Union of Geodesy and Geophysics (IUGG) (IUGG 2015 Resolution no. 2 2015), (IUGG 2023 Resolution no. 2, 2023). Predecessor gravity missions like the Challenging Minisatellite Payload (CHAMP) (Reigber *et al.* 2002), Gravity Recovery and Climate Experiment (GRACE) (Tapley *et al.* 2004), Gravity Field and steady-state Ocean Circulation (GOCE) (Drinkwater *et al.* 2003) and GRACE Follow-On (Landerer *et al.* 2020) have revolutionize our understanding of the global static and temporal varying gravity field and the related monitoring of mass transport processes, but also showed limitation regarding the achievable spatial and temporal resolution of resulting gravity field product, for example, Thomas *et al.* (2017), Rodell *et al.* (2018), Cazenave *et al.* (2019), Wouters *et al.* (2019) and Ciraci *et al.* (2020).

A new mission to improve the monitoring of hydrology, cryosphere, oceanography, solid Earth and climate change is therefore strongly anticipated. This evolution will provide enhanced continuity of science and services with respect to improving upon current capabilities and enabling novel science, applications and services. Achieving accurate purely satellite-based solutions on daily to weekly timescales was not possible with the previous generation of gravity missions. Indeed, at the moment this is only achievable in combination with models (Croteau *et al.* 2020). The Mass-change And Geosciences International Constellation (MAGIC), a collaboration between the European Space Agency (ESA) and the National Aeronautics and Space Administration (NASA) initiated over a decade ago, aims at fulfilling this new objective to improve current models and monitoring and in particular to introduce the capability to monitor and forecast extreme events like floods, droughts and other natural hazards.

The European Next-Generation Gravity Mission (NGGM), part of MAGIC, is currently in its Phase A Extension as first Mission of Opportunity in the ESA's FutureEO Programme. In the frame of the international cooperation, ESA and NASA have coordinated studies on gravity constellations to optimize the retrieval of mass change and transport in the Earth system. The new high spatio-temporal resolutions enable novel applications with the possibility to achieve short-term (or fast-track) gravity products in a subweekly basis. The collaboration aims at fulfilling the needs of international users communities, which are well expressed in the IUGG report from 2015 (Pail *et al.* 2015). The ESA/NASA Ad-hoc Joint Science Study Team contributed to the consolidation of mission requirements of the joint ESA/NASA MAGIC Mission Requirements Document (MRD, Haagmans & Tsaoussi 2020), where recommendations from the 2015 IUGG report (Pail *et al.* 2015) and the 2017 US Decadal Survey (Decadal Survey, 2017) were adopted. Further

recommendations based on previous work and studies (e.g. Bender *et al.* 2008; Iran Pour *et al.* 2015; Pail *et al.* 2019; Purkhauser *et al.* 2020), NASA/ESA Interagency Gravity Science Working Group (Visser *et al.* 2016) and the latest advances in satellite gravimetry were also incorporated in the MAGIC MRD.

The first pair (P1) of the MAGIC Constellation will be implemented via a NASA/German Aerospace Center (DLR) fast-paced cooperation to ensure continuity of observations. The second pair (P2) will be implemented by ESA, possibly with some NASA contributions. A staggered launch approach for the two satellite pairs should provide at least 4 yr of combined operations for MAGIC (Haagmans & Tsaoussi 2020). On NASA side, a Phase A study was initiated in 2023 March. On ESA side, since 2020 the NGGM/MAGIC concept is investigated in two parallel industrial Phase A studies complemented by a science support study <https://www.asg.ed.tum.de/en/iapg/magic/>. In the frame of the latter, several potential architectures and mission scenarios were investigated and numerically simulated to maximize the MAGIC's scientific return. The Bender-type double-pair mission concept (Bender *et al.*, 2008) and single/multiple pendulum configurations (Elsaka *et al.* 2013) were simulated in great depth. In these simulations, realistic error assumptions regarding the key payload products, in close interaction with the two parallel industry studies, were also implemented. In the frame of the science support activities for MAGIC, methodological improvements of processing strategies, optimum treatment of long-term signals and tailored post-processing techniques were also analysed (Abrykosov *et al.* 2021, 2022; Heller-Kaikov *et al.* 2023). The resulting simulations provided a clear overview on mission performance and scientific improvements enabled by MAGIC. Beyond the description of simulations setup and their improvement, which is available in Heller-Kaikov *et al.* (2023), this paper summarizes the initial results and recommendations from the ESA science study, and focuses on the scientific applications and the improvements expected to be achieved with MAGIC.

A brief introduction on analysed constellation scenarios and adopted methodology is given in Sections 2 and 3, respectively. In Section 4, the main results and comparisons with the MAGIC MRD requirements are shown and discussed. Section 5 presents the scientific impact and applications over a set of specific thematic fields: hydrology, cryosphere, oceanography, solid Earth, climate-change and geodesy. Conclusions and recommendations for ongoing and future work are finally provided in Section 6. It should be noted that, as result of technical and programmatic constraints, the current assumption for the MAGIC orbits is somewhat different than the cases presented in this paper and ongoing studies address such orbit configuration. However, the results presented are fully applicable but for minor aspects that will be described in later publications.

2 CONSTELLATION SCENARIOS

In the ESA Science Support study, the analysed orbits are based on the original candidate orbits provided in Massotti *et al.* (2021) and on a few additional scenarios which will be discussed here-

after. The main attention is often focused on the so-called 3d_H scenario, which is defined by a polar pair at 463 km mean altitude and 89° inclination, and a second pair at 432 km mean altitude and 70° inclination. The full list of analysed orbits is available in Appendix A. To study the impact of different periods of near-repeat orbits, or subcycles, and the influence of a change of altitude, several scenarios were defined. Beyond the Bender configurations, a few Sun-synchronous orbit (SSO) and pendulum concepts were also introduced. For all satellite pairs, the nominal intersatellite distance (ISD) baseline length is set to 220 km. For the scenarios 3d_H and 5d_LL additional satellite tandems were analysed, including in-line tandems with a baseline length of 100, 150 and 180 km, and pendulum pairs with angles of 15°, 30° and 45°.

Several potential mission architectures were investigated to narrow down the trade space of the constellation, especially to provide feedback to the parallel Phase A system industry studies, and to identify an optimum set-up regarding science return, technical feasibility and costs.

3 METHODOLOGY

The numerical closed-loop simulations performed to evaluate the compliance of various mission architectures to the given user requirements and their impact on applications are based on the full-scale gravity simulation software at the Institute of Astronomical and Physical Geodesy (IAPG), which is described in detail in Daras *et al.* (2015) and Daras (2016). The set-up of these simulations is described in detail in Heller-Kaikov *et al.* (2023) as summarized briefly in what follows. As a first step, orbits of the involved satellites are computed at a sampling rate of 5 s. The orbit scenarios underlying the simulations are summarized in the Table A1 in Appendix A. All orbits have specific subcycles: after a pre-defined period of time, the satellites come close to their initial (Earth-fixed) position, with a longitudinal shift as specified in the table, thus generating a homogeneous ground-track pattern within a given subcycle. All simulations refer to the period of time starting at 2002 January 1. Depending on the specific analysis, monthly (31 d), weekly (7 d) or short-term (3 d) solutions are computed. Normal equations are assembled and solved up to a maximum spherical harmonic (SH) degree/order (d/o) of 120, 100 or 70, depending on the retrieval period.

Regarding force (background) models in the closed-loop simulation, we distinguish between models used for forward modelling ('true world'), that is, computation of the orbits and simulation of the observations, and the gravity retrieval ('reference world'), that is, set-up of observation equations and observation residuals. For the forward modelling, the ocean tide model EOT11a (Savcenko & Bosch 2012) and the full atmosphere, ocean, hydrology, ice and solid Earth (AOHIS) signal given by the updated Earth System Model of ESA (Dobslaw *et al.* 2015) are used. For the computation of reference observations, the ocean tide model GOT4.7 (Ray 2008) is applied, meaning that we use the difference of the two ocean tide models EOT11a and GOT4.7 as a measure for the ocean tide background model error. In the case of the nominal processing scheme, the atmosphere and ocean (AO)-de-aliasing product and the corresponding error estimates (Dobslaw *et al.* 2016) are used in the inversion, such that "Hydrology, Ice and Solid Earth" HIS signals are retrieved. In both forward and backward modelling, the static gravity field model GOCO05s (Mayer-Gürr *et al.* 2015) is used, assuming that it is perfectly known. All background models extend up to d/o 120.

From the simulated orbits, synthetic High-Low (HL) and Low-Low (LL) Satellite-to-Satellite Tracking (SST) observations and residual observations are computed, using reference force models as described above. Product-noise models of the key instruments, laser ranging interferometer, accelerometers (ACC) and Global Navigation Satellite Systems (GNSS) receiver are superimposed (their models are assumed to include the effects of all the interactions with the satellite, e.g. those with estimation and control systems for attitude and thermal stabilization). These noise models are defined by Heller-Kaikov *et al.* (2023, ch. 2.1.2). The SH coefficients are retrieved by means of a standard least-squares parameter adjustment based on a Gauss–Markov model. The stochastic model is derived from pre-fit residuals of product-only noise simulations. Therefore, it is composed only of instrument errors and does not contain modelled temporal aliasing effects. The retrieval error $\Delta x = x - x_{\text{HIS}}$ characterizing the gravity retrieval performance of the considered simulated mission setup is computed as difference of the retrieved SH coefficients x and the SH coefficients x_{HIS} of the underlying 'true' mean HIS signal of the respective period of time. In order to visualize and compare the global retrieval performance of several scenarios, we compute the degree amplitudes of their retrieval errors Δc_{nm} and Δs_{nm} in units of equivalent water height (EWH, Wahr *et al.* 1998) according to

$$\sigma(n) = \frac{a\rho_e}{3\rho_w} \frac{2n+1}{1+k_n} \sqrt{\sum_{m=0}^n (\Delta c_{nm}^2 + \Delta s_{nm}^2)}, \quad (1)$$

where a is the semimajor axis of the Earth ellipsoid, ρ_e the mean density of Earth, ρ_w the density of water, k_n are the Love numbers and n and m represent the SH degree and order.

Detailed numerical studies have shown that the resulting performance scales with the retrieval period, respectively, the number of underlying observations N according to the Gaussian error propagation rule of \sqrt{N} . This does not only hold for product-only error cases including system measurement errors only, but also for the full-noise cases including also temporal aliasing errors (Pail *et al.* 2022).

4 RESULTS AND MATCH AGAINST MAGIC REQUIREMENTS

Fig. 1 shows a performance overview of the different constellation designs for a recovery period of 31 d as defined in Table A1 of Appendix A. These results, which are mainly based on the 3d_H scenario including realistic error models for the key instruments and tidal and non-tidal background model errors (*cf.* Section 3), clearly demonstrate the superior performance of Bender double-pair mission concepts over all other potential constellations, such as single-pair inline, SSO, or pendulum architectures. In case where the results include all error sources are labelled as 'full noise', whereas in case tidal and non-tidal background model errors are omitted they are labelled as 'product-only' solutions.

At this point it is to mention that following the approach from ESA NNGM and MAGIC MRD documents (Haagmans & Tsaoussi 2020), we use in this study unfiltered solutions as a performance metric. Any post-processing option would affect the mission performance in a different manner (different handling of omission and commission error, different leakage and smoothing effects, different signal dampening effects). Therefore, we consider the use of unfiltered solutions as the most unambiguous strategy. It is evident, that the difference between a single- and a double-pair solution will be

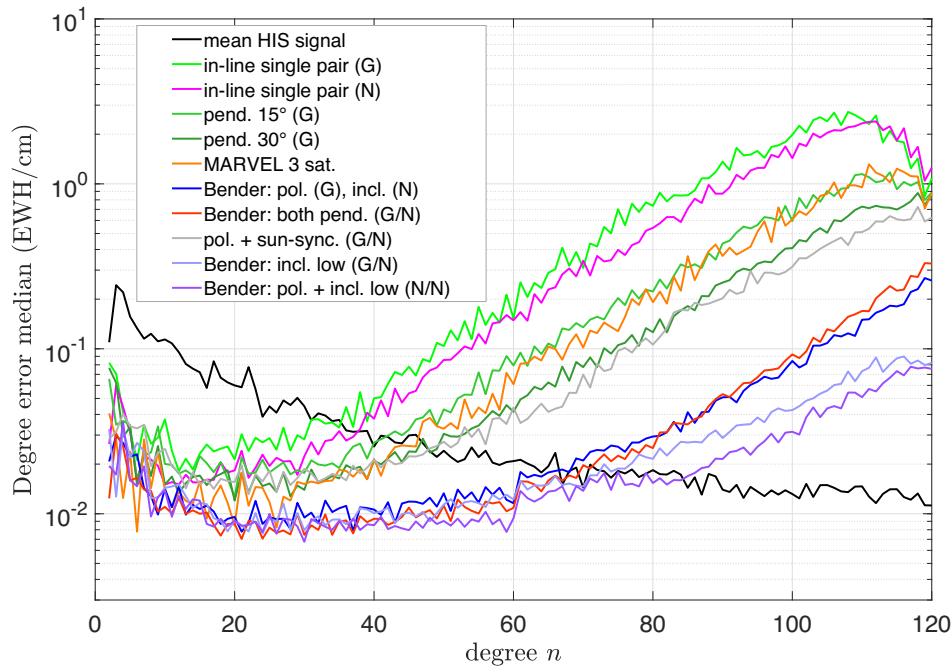


Figure 1. Degree error amplitudes of 31-d full-noise solutions from various mission constellations. ‘G’ means ‘SuperStar’ (GRACE-type) and *N* ‘MicroStar’ (NGGM/MAGIC-type) ACC performance. The numbers ‘15°’ and ‘30°’ refer to the opening angle of the pendulum formation.

largest for unfiltered solutions, because any type of filtering will attenuate the advantage of double pairs regarding their increased spatial and temporal resolution and their intrinsic improved de-aliasing capabilities. Impact studies based on post-processed solutions were performed, for example, by Hauk & Wiese (2020) and Wiese *et al.* (2022).

On top of previously mentioned benefits of flying in a Bender constellation, the altitude remains the main performance driver. In addition, in a double-pair scenario, the relative contribution of the inclined pair to the total performance is more than 90 per cent in the areas covered by both pairs (Pail *et al.* 2022; Zhou *et al.* 2021). Therefore, a low altitude together with high-performance instrumentation of the inclined pair is absolutely essential (Pail *et al.* 2022). The Science Support Study in the MAGIC Phase A has also analysed different ISD choices between satellites of the same pair. This distance represents a compromise between sensitivity (which improves with a longer distance) and spatial resolution (which degrades with greater distances). Based on performed simulations (Pail *et al.* 2022), ISD has an optimum for a distance of 200–250 km. For this reason, it is recommended for each pair to fly with in-line formations separated by 220 km, similar as realized on GRACE and GRACE-FO.

The simulated Level-2 gravity solutions demonstrate a pronounced gain using a double pair with respect to single pair GRACE-type scenarios, as notable in Fig. 2, showing the improvement ratios with respect to single pair. The greatest improvement can be seen for the ‘LL’ scenario (5d_LL, also labelled as ‘Bender: pol. + incl. low (N/N)’). This comes as an outcome of the altitude choice being the lowest among the represented architectures. Above SH degree 40–50, for most of the alternative scenarios, improvements can go beyond 10 times higher than single-pair GRACE-type configurations or high-altitudes scenarios. In the coefficient band around SH degree 80, where the signal-to-noise ratio (SNR) is close to one for two-pair constellations, the improvements are around 30 for Bender in-line scenario 3d_H compared to single-pair GRACE-type configurations.

The Level-2 mission performance of different architectures is compared against user requirements summarized in the MAGIC MRD (Haagmans & Tsaoussi 2020). Fig. 3 depicts the cumulative RMS curves for monthly full-noise solutions, while Fig. 4 for the product-only solutions. The product-only case includes the contribution of the measurement system error, which is defined as the uncertainty of Level-2 gravity field products solely resulting from satellite instrument inaccuracies and their coupling effects at satellite (or constellation) level but excluding all other effects (e.g. tidal, and non-tidal aliasing errors). The full-noise case includes the total effect of all error sources, including tidal and non-tidal aliasing errors. In Figs 3 and 4, the MAGIC MRD threshold and target Level-2 time-varying gravity field product requirements are also plotted. It is worth to note that these requirements are adopted from the IUGG report (Pail *et al.* 2015), with the remark that this reports defines user needs that can be fulfilled by post-processed (e.g. filtered) solutions. The IUGG user requirements are partially based on simulations with rather optimistic assumptions on AO background model errors, because only stochastic errors, but no deterministic (signal-related) error components were assumed. To obtain a more realistic assessment of the fulfillment of requirements, it would be also necessary to filter the solutions, which would reduce the cumulative errors. As defined above, this paper follows the approach from Haagmans & Tsaoussi (2020) in which the user requirements are answered by mission performance at Level-2 which guarantees consistent traceability to the user needs being as close as possible to the geophysical signal of interest, with the possibility of further satisfying user needs via higher level post-processed products. Therefore, the IUGG user requirements comparison against the MAGIC performance can be considered as conservative. In Figs 3 and 4, and in similar comparisons in this paper, post-processing was not applied in order to avoid alterations introduced by filters, which could make the comparison difficult to interpret afterwards. The mentioned points here above explain the breach of threshold requirements at low-to-medium SH degrees of the full-noise case in Fig. 3. The comparison of the cumulative errors with the IUGG requirements shows that in order to

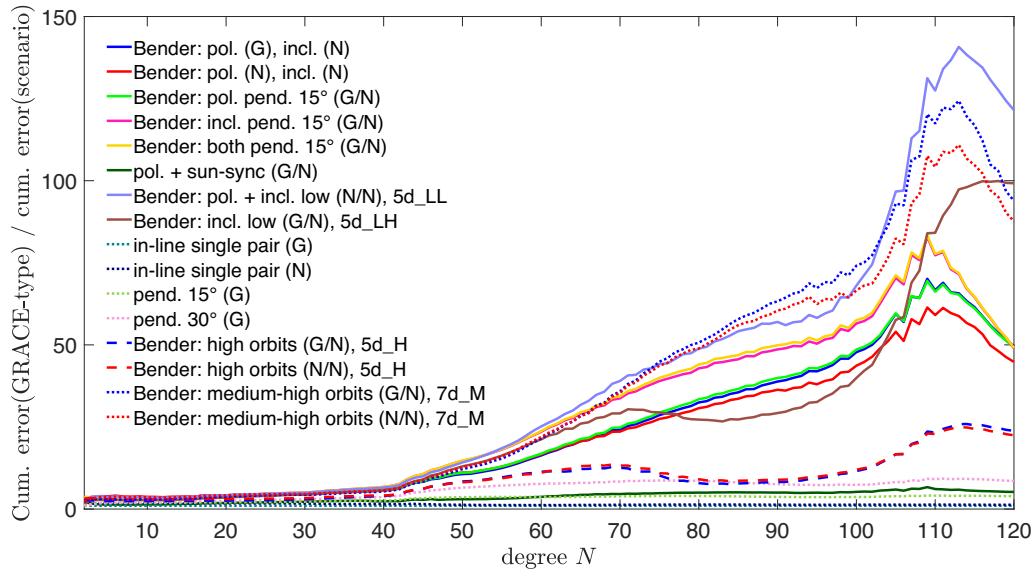


Figure 2. Ratio of the cumulative error curve of the GRACE-type single-pair and other full-noise simulated scenarios for a recovery period of 31 d. ‘High orbits’ and ‘medium-high orbits’ refer to 5d_H and 7d_M scenarios, respectively. The Bender scenario with both low altitude polar and inclined pairs refer to 5d_{LL}, while the double pair with low inclined pair consists of 5d_{LH}. The ‘15°’ and ‘30°’ numbers refer to the opening angle of the pendulum formation, the letter ‘G’ or ‘N’ refers to the GRACE-like and NNGM-like ACC noise assumptions. More details about orbit scenarios are available in Appendix A.

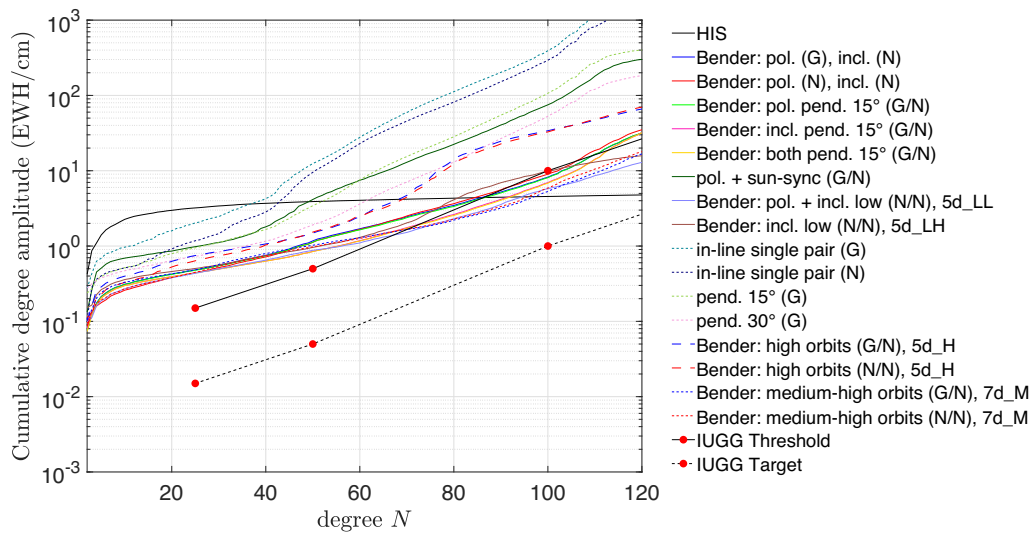


Figure 3. Cumulative RMS curves for the 31-d d/o 120 full-noise nominal simulation results, compared to the IUGG threshold and target requirements. For each individual scenario, the mean curve of the cumulative RMS curves of two subsequent 31-d solutions is shown.

meet threshold requirements and approach target requirements, a double-pair mission is required. The uncertainties of the single-pair and pendulum formations are too high to meet such requirements. The altitude turns out to have a particular influence especially for the performance at mid-to-high SH degrees. The scenarios using the 5d_H orbits (which have the highest satellite altitudes) perform poorly compared to 3d_H scenarios. The best performance is achieved by 7d_M and 5d_{LL} scenarios, which are characterized by low orbit altitudes. Pendulum formations do not provide a performance improvement with respect to the Bender constellations, and, moreover, they introduce a higher system complexity. Bender scenarios turned out to enable a relevant leap in performance compared to all other scenarios and to provide mission performance which satisfies the MAGIC MRD requirements except in the low-to-medium degrees.

Even if Figs 3 and 4 introduce raw simulations, already looking at current results, from a pre-operational standpoint, current EO-enabled services, such as those for land, climate, ocean and emergency management would largely benefit from improved mass-change data as available only from a constellation such as MAGIC (Massotti *et al.* 2022). Looking at the submonthly solutions and in particular at 7-d solutions (Figs 5 and 6), it is possible to find a similar behaviour with respect to the monthly solutions. In order to scale the monthly IUGG thresholds and targets to shorter retrieval periods, the requirements were scaled using a factor f_s

$$f_s = \sqrt{\frac{31}{r_p}}, \quad (2)$$

where r_p is the retrieval period in days. In Figs 5 and 6, for each scenario, the mean curve of the cumulative RMS curves of nine

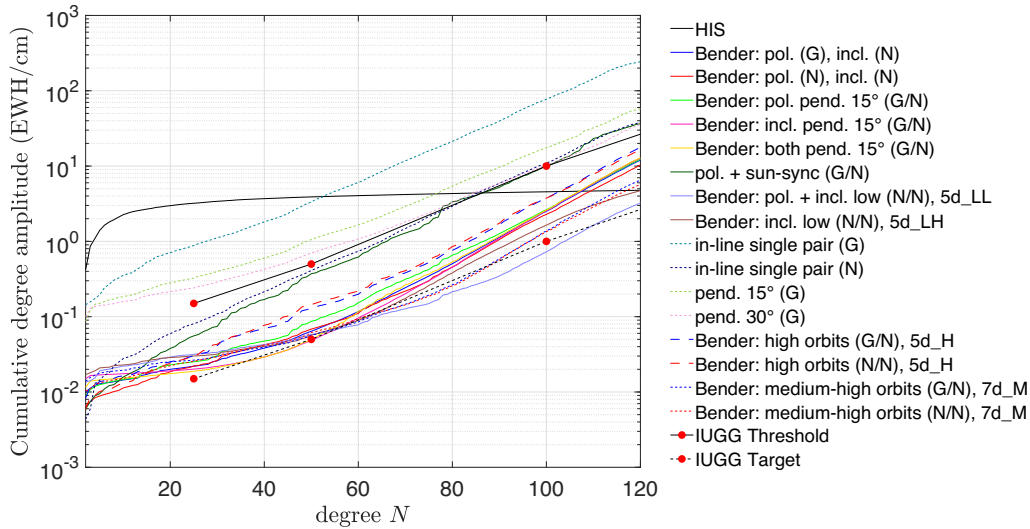


Figure 4. Cumulative RMS curves for the 31-d d/o 120 product-only simulation results, compared to the IUGG threshold and target requirements. For each individual scenario, the mean curve of the cumulative RMS curves of two subsequent 31-d solutions is shown.

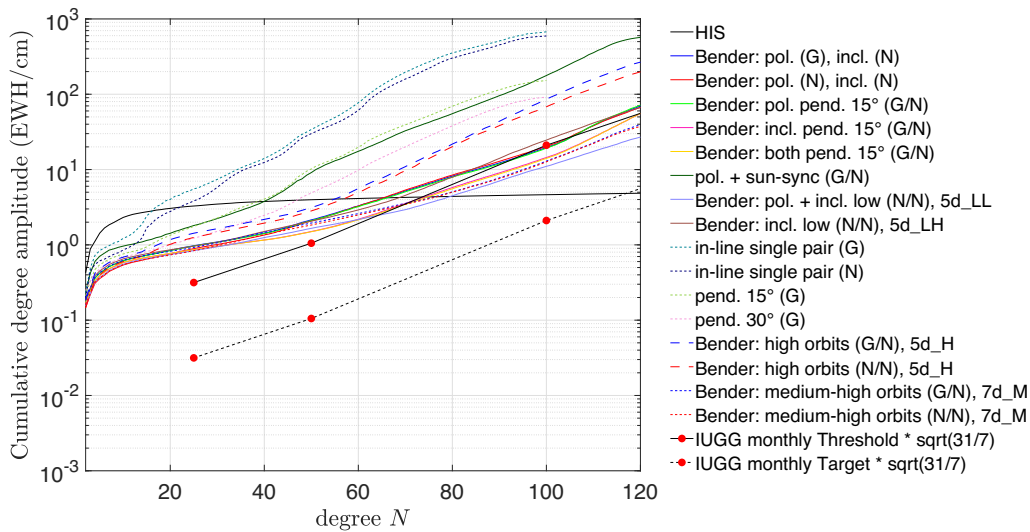


Figure 5. Cumulative RMS curves for the 7-d d/o 120 full-noise simulation results, compared to the IUGG threshold and target requirements.

subsequent 7-d solutions is provided. All simulations are generally computed up to a maximum SH d/o of 120. However, for the 7-d single-pair simulations, a reduced d/o of 100 was used because of the reduced ground-track coverage which would not allow to resolve the coefficients of larger SH degrees. It is evident that GRACE-type single-pair 7-d Level-2 solutions are dominated by noise from SH degree 20 onwards, whereas MAGIC scenarios of, for example, Bender in-line type have an SNR of one at SH degree 70. The reduced uncertainty offered by the MAGIC constellation allows for a wide use of 7-d Level-2 time-varying gravity products even with less need of post-processing by means of filtering.

5 SCIENCE AND APPLICATIONS

The purpose of this section is to describe the science impact analyses of the relevant mission scenarios in different fields of applications for the mass-change data, in particular in the fields of hydrology, cryosphere, oceanography, solid Earth, climate change and geodesy.

Sustained gravity field observations from space contribute significantly to a number of Essential Climate Variables (ECVs) as defined by the GCOS (Global Climate Observing System) programme. Among such variables, satellite gravimetry is a unique measurement technique which can retrieve global-scale data on ECVs such as ‘Groundwater’ and the newly adopted ‘Terrestrial Water Storage (TWS)’ (<https://gcos.wmo.int/en/essential-climate-variables/tws>). More specifically, satellite gravimetry can provide data services for the ECV products ‘Groundwater storage change’ and ‘TWS anomalies’.

5.1 Hydrology

One of the most common applications of satellite gravimetry is the analysis of time-series of water storage variations in hydrological units such as river basins or aquifers. These data provide fundamental information on the status of water resources, on pre-conditions and effects of hydrological extremes. Moreover, such data provide a valuable input for the closure of the water balance

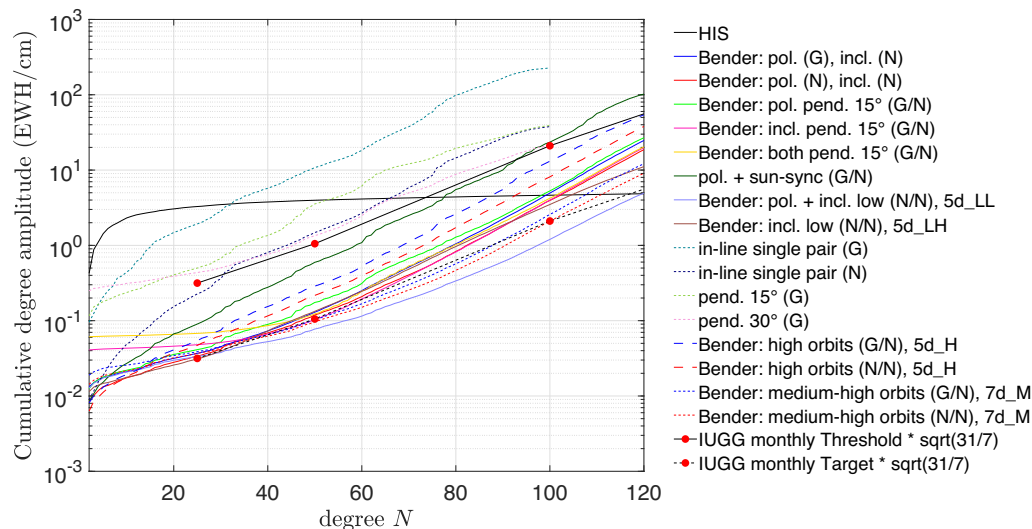


Figure 6. Cumulative RMS curves for the 7-d d/o 120 product-only simulation results, compared to the IUGG threshold and target requirements.

towards a comprehensive understanding of hydrological systems in response to climatic, environmental and anthropogenic changes. In spite of the unprecedented insights into hydrological dynamics that are achieved with GRACE and GRACE-FO, an even more widespread use of mass-change data in water cycle studies and water resources assessments is impeded by their low resolution. For many water management applications, for instance, the value of water storage information tends to increase with its higher spatial resolution and, thus, a better match with the size of the water management units of interest, such as catchments or aquifers can be reached.

To assess the benefit of MAGIC, 7-d simulation outputs of the scenarios 3d_H, 5d_Ma and 5d_Mb (listed in Appendix A), were compared to the results for a GRACE-like single-pair mission. Basin-average time-series of EWH for 52 weeks were derived for 405 individual river basins defined by the Global Runoff Data Center (GRDC 2020), representing the largest river basins worldwide. The temporal root-mean-square deviation (RMSD) between the reference signal (ESA ESM HI from Dobsław *et al.* 2015) and the simulation time-series was computed for each river basin to assess the accuracy of the simulation results. Following the MRD target and threshold values for envisaged uncertainties at specific spatial resolutions (Haagmans & Tsaoussi 2020), that is, 400 and 260 km for the monthly timescale in the thematic field of hydrology, the SH expansions were truncated at the degree corresponding to the desired spatial resolution, that is, $N = 50$ for 400 km and $N = 77$ for 260 km. The corresponding threshold uncertainties were derived from the monthly values by error propagation following eq. (2). This resulted in thresholds of 1.05 cm EWH for 400 km and 10.1 cm EWH for 260 km. In correspondence with chapter 4, unfiltered solutions are used to avoid the conclusions to depend on the choice of a specific filter. However, it should be noted that uncertainties of post-processed gravity field models to be later used for hydrological applications will be much smaller.

Fig. 7 shows the spatial distribution of RMSD values for all 405 river basins for the (a) GRACE-like mission and the MAGIC scenarios (b) 3d_H, (c) 5d_MA and (d) 5d_Mb. The improvement achieved by the MAGIC constellation is strongly visible. While the GRACE-like mission has maximum differences of more than 70 cm EWH for individual river basins and a global area-weighted

mean of 10 cm EWH, the MAGIC scenarios have maximum values in the range of 4–6 cm with area-weighted means of below 2 cm. Furthermore, the different error characteristics of the orbit constellations become evident. The 5d_Ma (i.e. a lower inclination of the inclined pair compared to 3d_H) and the 5d_Mb (i.e. a lower inclination of the polar pair) scenarios appear favourable for applications in continental hydrology in lower to mid-latitudes, as they show smaller residual on large parts of the continents, while the 3d_H scenario performs favourably in higher latitudes and polar regions.

A summary of the basin-average RMSD values is presented in the scatter plot in Fig. 8 (top), in which the RMSD for each of the 405 river basins is plotted against the basin size. Horizontal lines represent the MRD threshold uncertainty (1.05 cm EWH for 400 km resolution) and two additional thresholds (2.5 and 3.5 cm EWH). The vertical blue line represents the size of a spherical cap with 400 km diameter (about 125 600 km²) to roughly indicate the size of a river basin at this spatial resolution. It should be noted that this is only a rough approximation as river basins may largely deviate from a spherical shape. Signals of river basins below this size are difficult to isolate from the surroundings. It can be seen that the uncertainty requirement of the MRD can hardly be fulfilled by the unfiltered 7-d solutions for any of the river basins, including the largest ones. However, this is not surprising as the MRD thresholds were introduced for post-processed solutions. Nevertheless, also this scatter plot again stresses the strong improvement of MAGIC over a single-pair mission. Fig. 8 (bottom) shows the ratio of the RMSD of the latter compared to the MAGIC 3d_H scenario, with ratios larger than 20 especially for very small river basins. For basins around an extent of 400 km, that is, degree $N = 50$, the improvement by MAGIC is between 5 to 15 times. Only for very large river basins, in which the additional smoothing imposed by calculating the basin-average reduces most of the noise in both GRACE-like and MAGIC scenarios, the ratio gets smaller.

For higher spatial resolutions than 260 km (i.e. truncation at degree $N = 77$), the threshold uncertainties provided in the MRD appear to be more relaxed, as they can be reached by all the MAGIC scenarios for most river basins (not shown). The only exceptions are basins with an area smaller than the one corresponding to a spherical cap of 260 km diameter, which are likely below the achievable

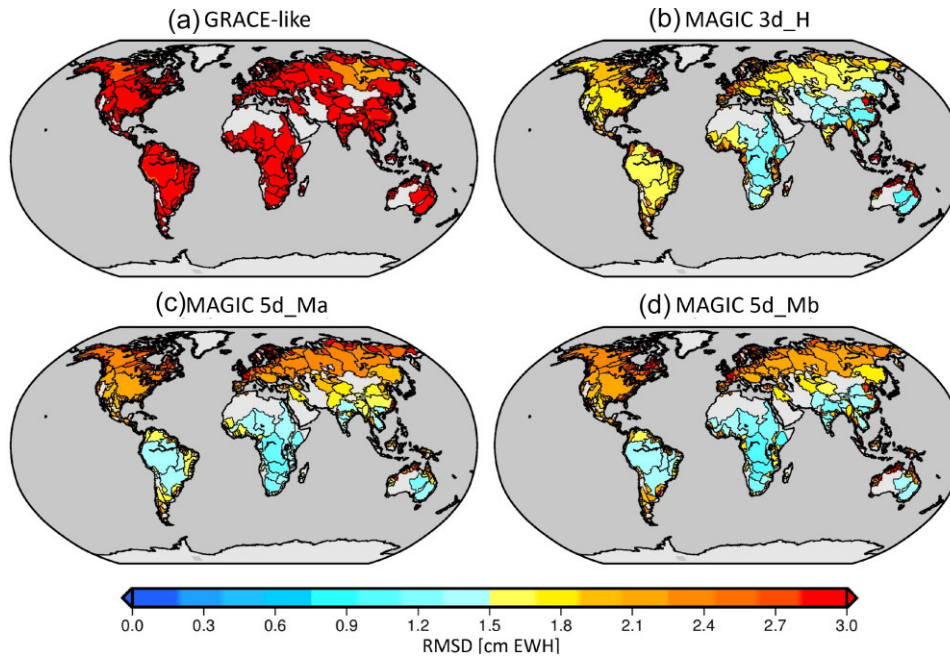


Figure 7. Temporal RMSD of basin-average water storage variations for 7-d simulation output (a: GRACE-like scenario, b: MAGIC 3d.H, c: MAGIC 5d.Ma and d: MAGIC 5d.Mb) relative to the ESM HIS reference signal, truncated at degree $N = 50$ (i.e. 400 km spatial resolution) for 405 GRDC basins.

spatial scale. A summary of the statistics for both spatial resolutions (400 and 260 km) is provided in Table 1. The threshold accuracy currently given in the MRD for hydrological applications at a comparatively high spatial resolution (10.1 cm EWH at $N = 77$) can be fulfilled by MAGIC 3d.H (and similarly by 5d.Ma and 5d.Mb) for more than 90 per cent of the 405 major river basins worldwide when considering unfiltered solutions. Even higher accuracies that may be required for several hydrological applications can be met in a large number of basins (Table 1, right columns). In contrast, the current MRD at the lower spatial resolution of 400 km cannot be met by MAGIC for any river basin. However, relaxing this threshold to 2.5 or 3.5 cm EWH, which can be expected to be still acceptable for many hydrological applications, will allow for resolving TWS variations in 67 and 90 per cent of the investigated river basins, respectively (*cf.* Table 1). With a GRACE-like mission this would not be possible, as even for these more relaxed numbers the RMSD for almost none of the basins stays below the thresholds. Furthermore, accuracy expectations for post-processed gravity field solutions are much higher, therefore the numbers listed above should be regarded as a relative performance improvement and not as the final uncertainties achievable with a double-pair mission for hydrological applications.

5.2 Cryosphere

The launch of GRACE in 2002 provided a breakthrough in our understanding of the glaciated regions. For the first time, mass changes of the ice sheets and glaciers could be measured directly, which revealed an imbalance of both ice sheets and all other major glacier systems (e.g. IMBIE 2020, 2018; Ciraci *et al.* 2020; Wouters *et al.* 2019) and provide an invaluable data set for calibration and validation of ice sheet models (e.g. Fettweis *et al.* 2020; Schlegel *et al.* 2016). Despite the major advances, there remains a strong demand for future improvements, to allow attribution of mass signals to individual glaciers and drainage systems, reduce signal contamination

by hydrological and oceanographic mass variations, and improve the resolution and accuracy of data combination approaches (e.g. with altimetry, GNSS and other complimentary data, Pail *et al.* 2015). A future mission should therefore not only continue the current time-series, especially relevant for the ice sheets where an interplay of short and multidecadal to centennial timescales is at play, but also provide an increased spatial resolution at increased accuracy. Although the GRACE/GRACE-FO missions provide us with a clear picture of the current imbalance of the ice sheets as whole and their major subregions, many of the relevant processes causing this imbalance have spatial scales which remain unresolved in the current space-borne gravimetric observations. On Greenland (GrIS), mass loss occurs predominantly around the margins of the ice sheets. In this ablation zone, runoff of summer melt water exceeds snow accumulation, which is counteracted by a net mass gain in the interior accumulation zone. The dominant processes in these two zones are very different from a physical point of view (Noël *et al.* 2019). In Antarctica (AIS), the limited spatial resolution precludes us to properly separate the mass changes on the eastern and western sides of the warming Antarctic Peninsula, and of individual glacier systems in the rapidly changing Amundsen Sea Embayment.

Here, we assess the performance in mass-change applications related to the cryosphere of different mission configurations, that is, the one single GRACE-type pair scenario, and three Bender double-pair scenario with varying altitudes and inclinations of the polar and inclined pair (3d.H, 5d.Ma and 5d.Mb). We focus on the ice sheets of GrIS and AIS, which were each subdivided into smaller regions, based on ice prominence, flow direction of the ice, and climatological settings. For AIS, the basin definition of Zwally *et al.* (2012), was used, dividing the ice sheet into 27 regions. For GrIS, six regions were defined based on Sasgen *et al.* (2012). In GrIS, these regions were further subdivided into the ablation and accumulation zone (approximated using the 2000-m elevation contour), yielding 18 regions in total. In AIS, surface melt contributes minimally to

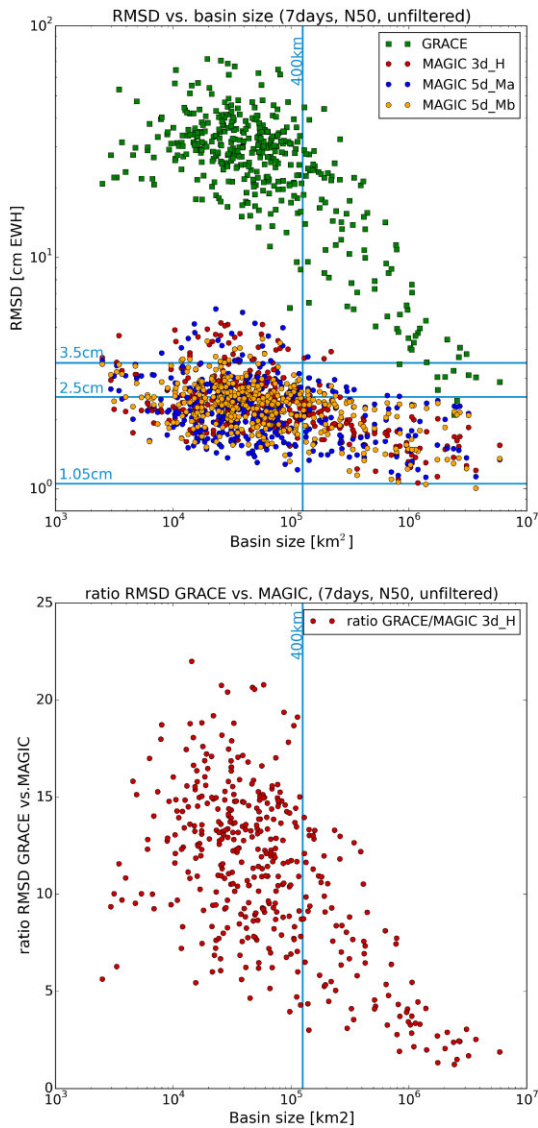


Figure 8. Top: scatter plot of RMSD of basin averages of water storage variations for 405 GRDC river basins truncated at $N=50$ plotted against basin size. Blue horizontal lines indicate different uncertainty thresholds of 1.05 cm (i.e. the MRD threshold requirement), 2.5 and 3.5 cm EWH. The vertical blue line represents the area of a spherical cap with 400 km diameter. Bottom: ratio of the RMSD of a GRACE-like constellation versus the RMSD of MAGIC 3d_H constellation for each river basin.

mass changes, hence, a similar subdivision of the regions was not made for this ice sheet.

To retrieve the mass variations of the ice sheets and their (sub)regions, two approaches were used. First of all, the method of Wouters *et al.* (2008), in which the SH are transformed to surface mass loading anomalies. Subsequently, modelled mass anomalies in the (sub)regions are adjusted iteratively, until convergence is reached with the input mass anomalies from the simulation. Secondly, the mascon approach of Ran *et al.* (2018) synthesizes gravity disturbances at pre-defined points positioned at a specific satellite altitude, which are then converted into localized mass anomalies through a linear functional model which uses the variance-covariance matrix in its weighting. Since both methods yielded comparable results, it was decided to proceed with the method of Wouters *et al.* (2008) for computational efficiency.

To assess the performance of the different mission configurations, the time-series of mass variations retrieved from the simulations were compared to the truth signal, retrieved from the HIS model from Dobsław *et al.* (2015, i.e. without the noise component, provided up to degree/order 180). Time-series for all basins were plotted for a qualitative assessment. For a quantitative analysis, the root-mean-square error was computed based on the difference between the simulated and truth time-series and compared to the relevant threshold and target user requirements in the MRD (Haagmans & Tsaoussi 2020). As for the hydrology case study (Section 5.1), the weekly, unfiltered SH expansions were truncated at the appropriate degrees N and the monthly threshold (5.5 and 50 cm EWH at 250 and 150 km, respectively) and target uncertainties (0.55 and 5 cm EWH at 250 and 150 km, respectively) were scaled using eq. (2). This results in threshold/target values of 11.6/(1.2) cm EWH at 250 km resolution ($N = 80$), and 105/(10.5) cm at 150 km resolution. For the latter, we use the maximum provided degree of $N = 120$ for the MAGIC-scenarios and $N = 100$ for the single GRACE-type pair scenario.

Figs 9 and 10, and Table 2 summarize the performance of the four configurations with respect to the threshold and target criteria for a spatial resolution of 250 km, at monthly timescales. Most notable is the improved performance of the Bender constellations with respect to a single-pair mission in the lower latitude basins of the two ice sheets, a consequence of the addition of the inclined pair. For configuration 5d_Mb, the threshold is met for 40 out of the 45 basins. As can be seen in Fig. 10, basins not passing the threshold for this configuration generally have areas smaller than approximately 62 500 (250×250) km². On GrIS, the threshold is met for all basins, except for the accumulation zone of the northernmost region 1, where the RMSD is just 1 mm above the threshold. In AIS, the basins exceeding the threshold are all located on the Peninsula (basins 24–27). For the 5d_Ma and 3d_H configurations, the threshold is exceeded for larger basins, at approximately 200 000 km². The 3d_H configuration performs slightly better than 5d_Ma, with basins 32 and 29 passing the criterion, respectively. Still, both outperform a single-pair GRACE-like configuration (20 basins), although both these configurations result in an increased RMSD in the lower elevation zones of the northernmost basins of GrIS (1, 2 and 6), compared to the single-pair results (Fig. 9). This is a consequence of an artifact at the transition zone between the two pairs for the constellation cases caused by non-optimal gravity field recovery processing, and is a subject of future investigations. The effect is related to the fact that in the transition zone, going from lower to higher latitudes, the data density at $\pm 70^\circ$ latitude is changing abruptly from a dense ground-track sampling of the constellation to a lower ground-track sampling of the polar pair. Together with different noise assumptions for the polar and the inclined pair, this can cause numerical issues in the transition zone. Strategies and alternative relative weighting schemes are currently investigated to solve this issue (Pail *et al.* 2022). When considering the target criterion, very few basins pass, none of them located on GrIS. Again, the 5d_Mb configuration performs best, but even there only 5 out of 45 basins meet the requirements.

When considering a higher spatial resolution of ~ 150 km (maximum degree/order 120), the RMSD increases for all basins for the 5d_Ma constellation, indicating that the higher coefficients carry little signal information. For the 5d_Mb and 3d_H scenarios, a reduction of up to 40 per cent RMSD is observed in several basins (AIS basins 1, 3, 8, 9, 17, 24, 25 and 26, and the GrIS lower elevation basin 6). When considering the bulk basin statistics, similar conclusions hold as for the 250 km resolution. Again, the 5d_Mb configuration

Table 1. Number of river basins for which the RMSD values of water storage variations are below given thresholds for two different spatial resolutions (400 and 260 km), each for the GRACE-like and the MAGIC 3d_H scenarios, relative to the ESA ESM reference.

Threshold [cm EWH]	400 km, $N = 50$		Threshold [cm EWH]	260 km, $N = 77$	
	No. of basins 3d_H	No. of basins GRACE		No. of basins 3d_H	No. of basins GRACE
3.5	90% (366/405)	2.5% (10/405)	10.1	91% (370/405)	2.5% (10/405)
2.5	67% (270/405)	0.5% (2/405)	6.1	67% (273/405)	0.5% (2/405)
1.05	0% (0/405)	0% (0/405)	2.5	17% (69/405)	0% (0/405)

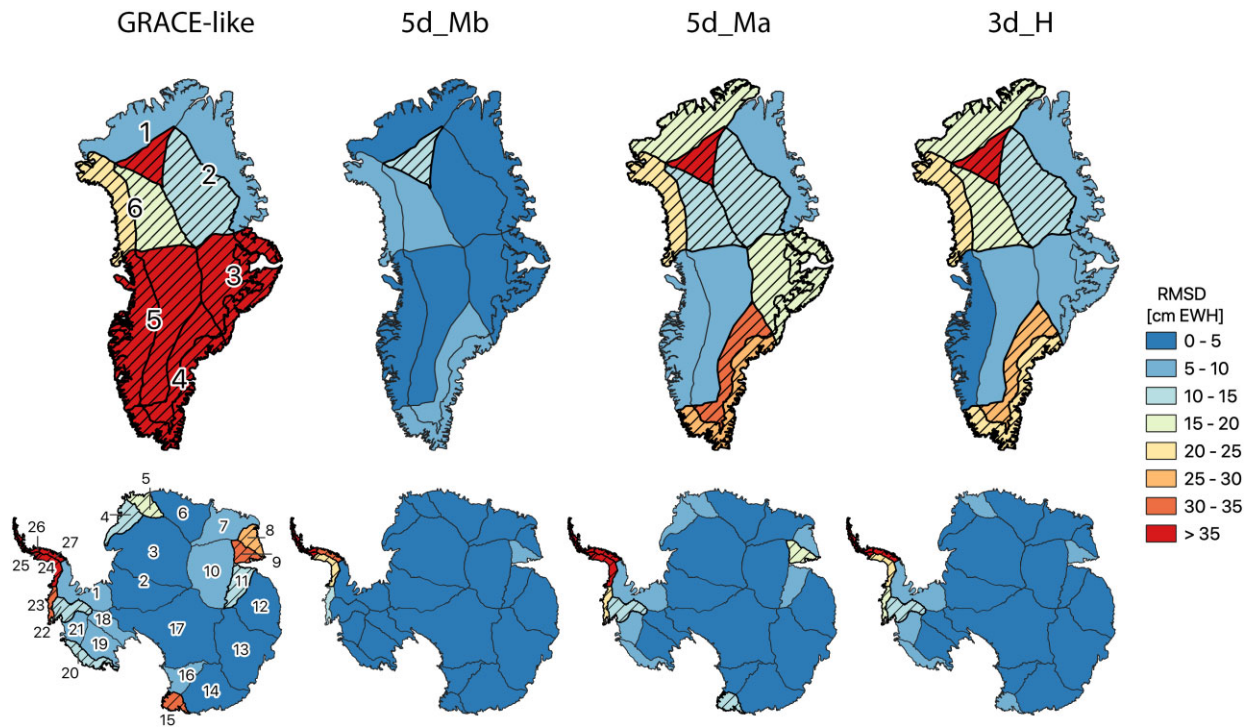


Figure 9. Temporal RMSD of 7-d simulation output for the four considered constellations and reference solution truncated at degree $N = 80$ (i.e. 250 km spatial resolution) for GrIS (top) and AIS (bottom) basins. In the hatched areas, the RMSD exceeds the threshold value.

performs best, with all 45 basins meeting the (comparatively less stringent) threshold criterion of 50 cm RMSD. Configuration 3d_H performs almost equally well (44 basins), although it should be noted that the RMSD for most basins lies above that of 5d_Mb. The 5d_Ma and the single-pair, GRACE-like configurations show a comparable performance, in terms of number of basins passing the criterion. Compared to the 250 km results discussed earlier, more of the basins also meet the target criterion, with 5d_Mb configuration again outperforming the other constellations.

To illustrate how each of the mission scenarios may improve our understanding of the mass balance of the GrIS and Antarctic Ice Sheet, we show time-series of mass anomalies in the lower elevation zone of GrIS basin 5 and the northern part of the AIS Peninsula (basins 25 and 26) in Fig. 11. In the single-pair, GRACE-like scenario, the typical mass-loss signal following summer melt is obscured by noise. In the Bender configurations, the HIS *truth* signal is accurately tracked by the simulations, with an RMSD reduction of up to 99 per cent for the 5d_Mb scenario. Irrespective of the chosen configuration, resolving mass redistribution in basins 25 and 26 on the Northern Antarctic Peninsula remains a challenge. These elongated geographical features have a typical width in the range of 50–100 km, well below the targeted resolution of a future mission. When retrieving mass changes, this will cause signal leakage from

one basin to the other, thereby increasing the RMSD. However, when combining the two basins, this leakage error cancels out and the RMSD drops to an order of magnitude lower than what is currently achievable with a single-pair mission.

5.3 Oceanography

Ocean bottom pressure is an unusual and uniquely valuable parameter for monitoring ocean dynamics, because it is so strongly controlled by the ocean bottom topography that it filters out many of the small-scale dynamics (the ocean mesoscale) which dominate sea level variability and most other quantities (Hughes *et al.* 2018). This results in a mix of different behaviours: some abyssal plain regions, especially near energetically eddying regions, are still dominated by the mesoscale. Others show coherent variability over the entire basin (enclosed by a depth contour). Above about 3000 m depth, the ocean sidewalls show highly coherent variability (often over tens of thousands of kilometres) along depth contours, but significant structure across contours, effectively integrating the ocean circulation, and providing an efficient means to monitor the climatically important meridional overturning circulation (MOC, Hughes *et al.* 2018). A secondary result of this strong dynamical control is that bottom pressure signals tend to be small compared

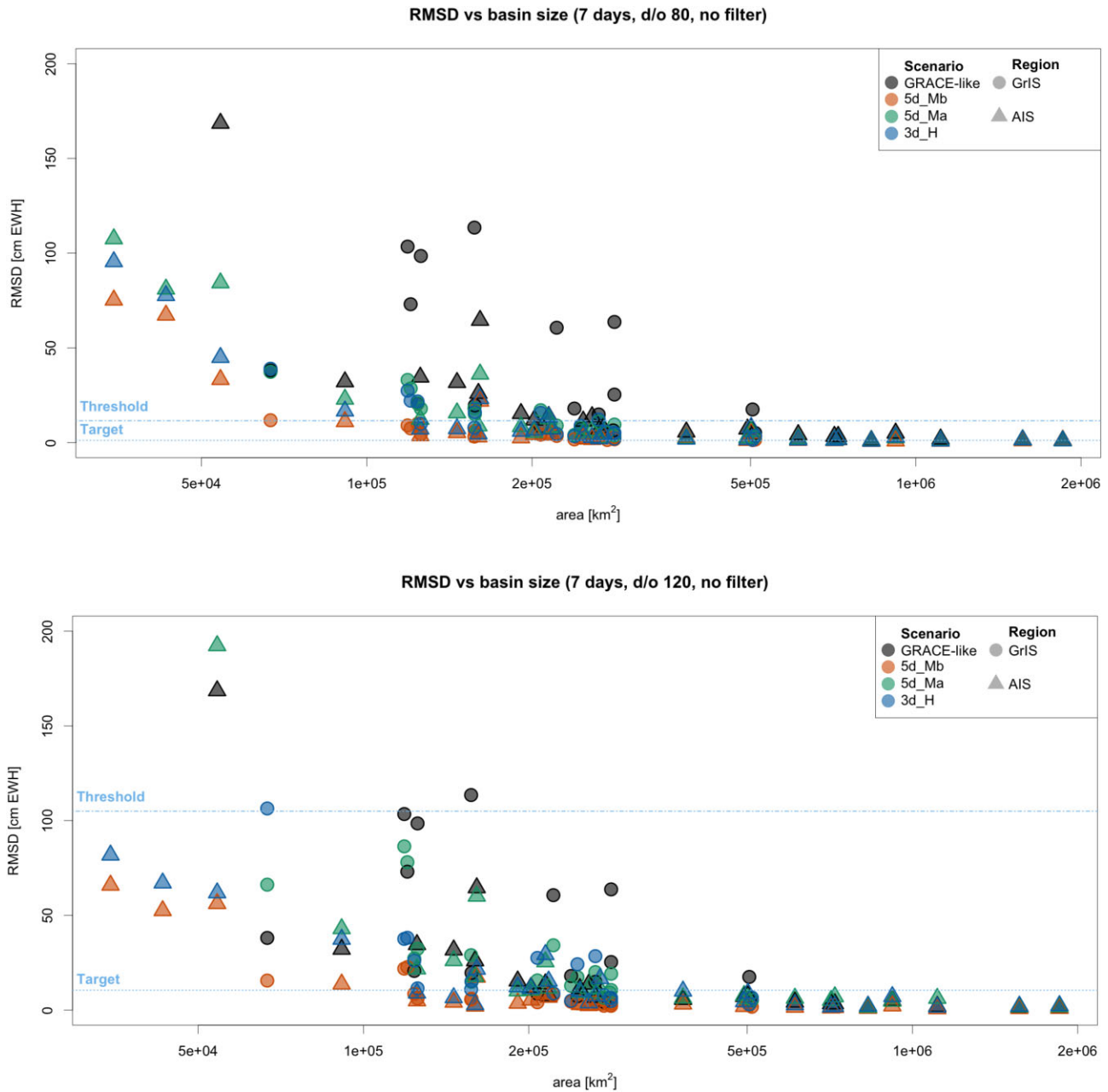


Figure 10. Top: RMS difference for each of the GrIS (dots) and AIS (triangles) basins as a function of their area, for all four configurations. Only coefficients up to degree/order 80 were used, corresponding to a spatial resolution of approximately 250 km. The dotted and dashed–dotted line indicate the (scaled) target and threshold RMS criteria at monthly timescales, respectively. Bottom: as the top figure, but for coefficients up to degree/order 120.

Table 2. Number of basins of the GrIS and AIS ice sheet for which the monthly threshold and target criteria are met for the four different configurations, using coefficients up to degree/order 80 and 120, corresponding to a spatial resolution of 250 and ~150 km, respectively.

Configuration	250 km ($N = 80$)				~150 km ($N = 120$)			
	Threshold (11.6 cm EWH)		Target (1.2 cm EWH)		Threshold (105.0 cm EWH)		Target (10.5 cm EWH)	
	GrIS	AIS	GrIS	AIS	GrIS	AIS	GrIS	AIS
GRACE-like	5 / 18	15 / 27	0 / 18	2 / 27	17 / 18	24 / 27	5 / 18	14 / 27
5d_Mb	17 / 18	23 / 27	0 / 18	5 / 27	18 / 18	27 / 27	15 / 18	22 / 27
5d_Ma	10 / 18	19 / 27	0 / 18	3 / 27	18 / 18	24 / 27	4 / 18	15 / 27
3d_H	11 / 18	21 / 27	0 / 18	3 / 27	17 / 18	27 / 27	8 / 18	17 / 27

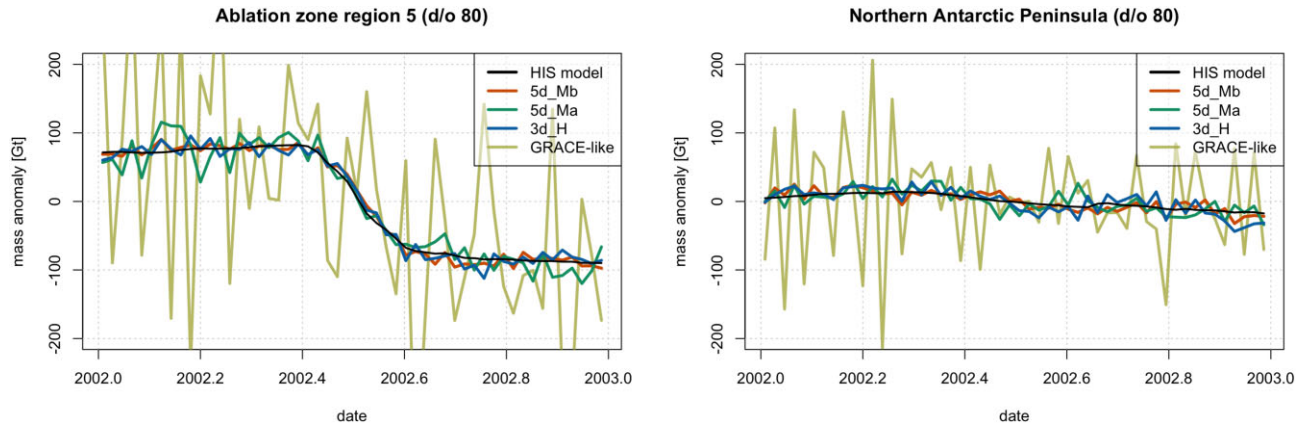


Figure 11. Mass variations in the low-elevation zone of GrIS basin 5 (left) and Northern Antarctic Peninsula (basins 24 and 25; right) simulated by the HIS model and retrieved from the four mission configurations simulations using the method of Wouters *et al.* (2008).

to sea level, and hence challenging to measure from space. We will express bottom pressures in cm water equivalent (cm EWH, very close to mbar, or hPa), and use the $(1/12)^\circ$ resolution NEMO ocean model described in Hughes *et al.* (2018) to investigate the signals.

To illustrate the capabilities of a future mission, we choose two target signals representing a coherent basin and an MOC signal. The coherent basin example is taken from the Caribbean Sea (Hughes *et al.* 2018), a mode with dominant period of 120 d, but significant variability at other periods (standard deviation 1.56 cm EWH overall, or 1.14 cm EWH using a narrow-bandpass filter).

Fig. 12(a) shows the results of this analysis, using truncation at different SHs to illustrate the scale dependence. The analysis attempted to reconstruct 54 yr of weekly values from NEMO, by convolving (NEMO plus noise) fields with the averaging kernel shown in Fig. 12(b). The noise was taken from the 3d_H scenario, and from a standard GRACE-like scenario (one year of weekly values, repeated each year). We also repeated the analysis with noise divided by $\sqrt{4} = 2$, which would approximate the effect of monthly averaging if there were no high-frequency signal; with no noise (only truncation); and with all time-series reduced to 4-week means. The result of truncation in the no-noise case is, as well as adding noise from leakage, to reduce the amplitude of the detected signal due to smoothing of the averaging kernel. To correct for this effect, a least-squares fit of the time-series at each truncation on the target ‘true’ time-series was used to derive an optimal scaling factor at each truncation. This same factor (a function of harmonic degree) was applied to all other cases, thus amplifying the noise as well as the signal.

We see that the low-degree harmonics do a poor job, and actually contaminate the signal in most cases. Explained variance starts to grow only after a scenario-and-noise-dependent harmonic degree is reached, and peaks at about degree 25 for the GRACE-like scenario, and about degree 60 for Bender scenarios. The corresponding averaging kernels at these degrees are shown in Figs 12(c) and (d). There is significant leakage outside the basin at degree 25, and much better localization at degree 60.

In this simulation, the GRACE-like scenario can never produce a useful signal, but the Bender case explains 20 per cent of weekly variance, rising to 50 per cent for monthly values, though still short of the 80 per cent predicted for 4-week averages should the signal have no higher frequency variability. The Bender case is thus a dramatic improvement over the GRACE case.

In both cases, however, these are pessimistic estimates. It is known (Hughes *et al.* 2016) that, with carefully designed filtering, GRACE can reproduce about 40 per cent of the signal variance for data bandpassed around 120-d period. The low-degree problems are probably mitigated by more careful processing design, as they would also be for MAGIC or, indeed, any other missions. However, the main conclusion of a large like-for-like improvement over a single-pair mission, and detection of a small-basin signal with amplitude around 1 cm EWH, remains clear.

A similar analysis was undertaken for the North Atlantic MOC. The MOC is measured in sverdrup (Sv) where $1 \text{ Sv} = 10^6 \text{ m}^3 \text{ s}^{-1}$, and Fig. 13(a) shows a time-series of 54 annual-mean values of the overturning at 43° N . A particular difficulty in this case is the potential for incidental correlations associated with large-scale processes. The dynamical signal associated with the MOC is known to be related to pressures on a narrow strip of continental slope, at the ocean’s western boundary, a positive MOC anomaly in the North Atlantic being associated with negative pressure anomalies in shallow water, and positive pressure anomalies between about 1200 and 3200 m depth (Elipot *et al.* 2014; Hughes *et al.* 2018). However, pressures may be correlated over a much wider region, perhaps due to a genuine dynamical connection, but perhaps also as a result of signals with common forcing, or time-series with few degrees of freedom. To be sure that we are measuring the MOC itself, rather than other dynamics that are often associated with the MOC, we must take care to limit the signal to the continental slope region alone. With associated pressure signals of order 1–3 cm EWH (Hughes *et al.* 2018), this thin region makes a challenging target.

The model MOC time-series (standard deviation 1.6 Sv) is dominated by a rise from 1959 to 1993, and a fall thereafter. This long-term signal is associated with many other global changes, including basin-average pressure changes in the Atlantic and Pacific, which means it can be reconstructed with large-scale averages. Accordingly, we have also used an ‘interannual’ version of the time-series, in which a running decadal mean has been subtracted (blue curve in Fig. 13a; standard deviation 0.72 Sv) to reduce the chance of incidental correlations.

Our target averaging kernels for the two time-series are shown in Figs 13(b) and (c). These were constructed by limiting to the region shown, and to depths shallower than 3200 m on the continental slope, fitting the MOC on the equivalent time-series of bottom pressure at each gridpoint, and multiplying by the squared correlation to reduce

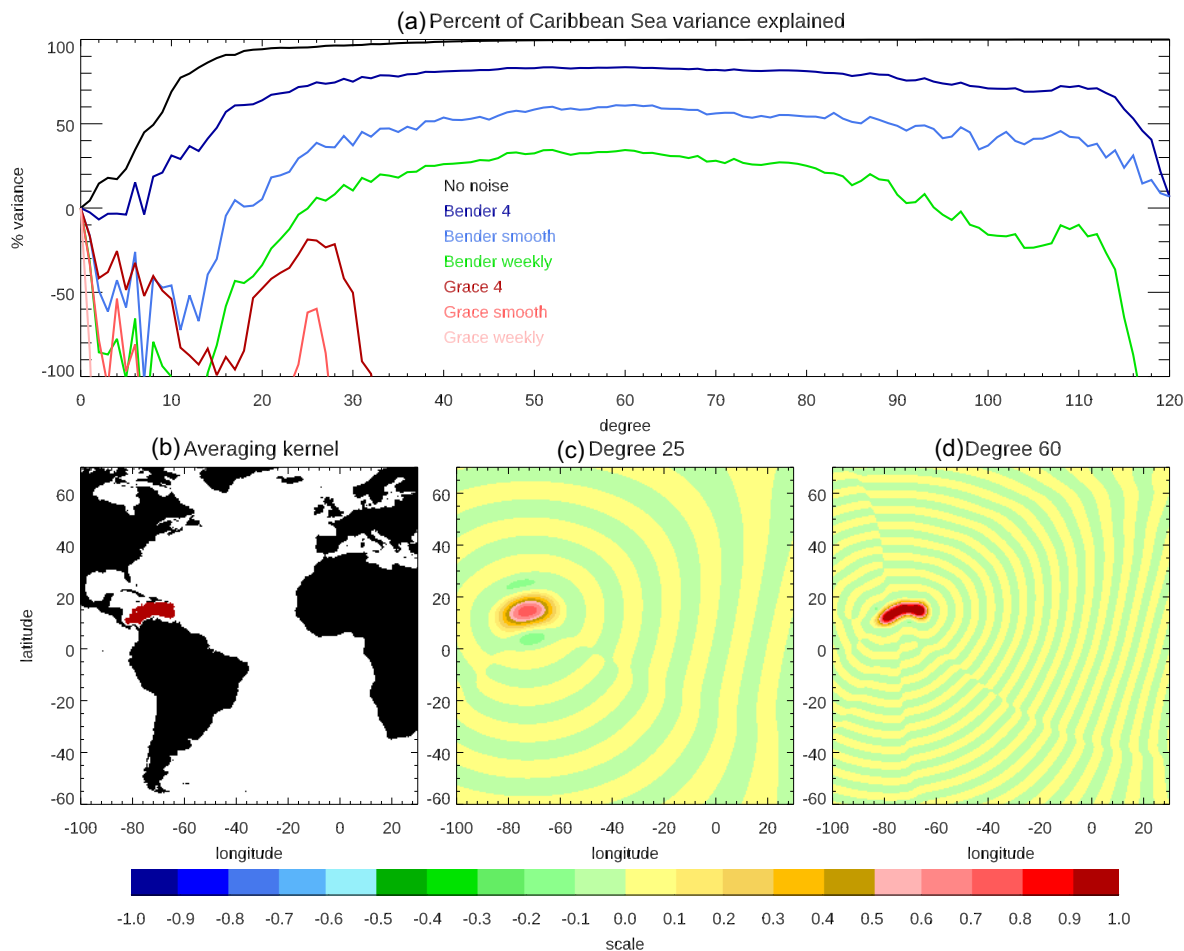


Figure 12. Retrieval of the basin-averaged bottom pressure from the Caribbean Sea, simulated under the 3d_H scenario and equivalent GRACE-like mission. Noise is taken from the weekly retrievals minus the scenario ‘truth’, and signal from the NEMO ocean model. (a) The percentage of the time series variance explained after truncating at different SH degrees, with the noise set to zero (‘no noise’), with full-noise (‘weekly’), with the weekly noise divided by $\sqrt{4} = 2$ (‘4’), and with 4-week averages used throughout (‘smooth’). (b) The averaging kernel (relative gridpoint weightings per unit area). (c) The kernel after truncating at degree 25, and (d) at degree 60.

the weighting for poorly correlated regions. The result is certainly not the optimal method of reconstructing the MOC, but it provides a realistic target function with the expected spatial characteristics.

As we are now using annual values, and only have noise estimates for weekly values, we divide the noise fields by $\sqrt{52}$ to simulate the noise for annual means (as noted at the end of Section 3, this scaling appears to be quite effective). We also, far more speculatively, use a scaling by a factor $\sqrt{520}$ to represent decadal means. This undoubtedly omits significant systematic errors on these timescales, but is presented as an aspirational outcome for long-period monitoring (decadal changes of the MOC are the most climatically interesting).

The difference between the fidelity of the two reconstructions (Figs 13d and e) is very informative. The large percentage of variance apparently explained by low-degree gravity fields in the long-term case is clearly not representing a signal limited to the continental slope, but rather is the leakage of the larger-scale signal into the filtered averaging kernel.

For the interannual case, the rise in variance explained with degree, for the no noise case, is a much more plausible description of how well the kernel is realized at different resolutions. In this case, GRACE scenarios are of limited use, but the Bender case (blue)

reproduces 50 per cent of the time series variance at degree 60. While the ‘decadal noise’ case may be too optimistic, it is worth noting that it is roughly equivalent to seeking a signal $\sqrt{10}$ times larger than the model variations (2.3 Sv rather than 0.72 Sv), and that this is a perfectly reasonable size for expected MOC changes due to climate change.

There have already been attempts at using GRACE data to measure MOC changes (Delman & Landerer 2022), with some success. It seems clear, however, that these rely on there being auxiliary signals at larger length-scales than those on the continental slope that are known to be dynamically related to the MOC (Elipot *et al.* 2014; Hughes *et al.* 2018). The higher resolution capability of a Bender configuration, providing useful extra information out to at least degree 60 and potentially about degree 85 for larger signals, is a step change of resolution with important consequences for ocean monitoring. It leads to the possibility of genuinely isolating the continental slope signal at an accuracy which is comparable to the best *in-situ* measurement systems (McCarthy *et al.* 2020), which are themselves only representative of single latitudes, rather than of the broad latitude range that is of relevance to climate change.

5.4 Solid Earth

We have investigated to what extent a Bender configuration (3d.H) detects the coseismic gravity signal generated by a smaller earthquake compared to a GRACE-type single-pair scenario. The coseismically generated seismic waves are covered globally at magnitude $M 5$ or even $M 4.5$ by existing international seismic networks, that provide the hypocentre and fault plane, and solution of the seismic moment. Problematic is the detection of post-seismic deformation as well as the intermediate phases in the earthquake cycle which give origin to a crustal deformation and a gravity signal, but do not generate seismic waves detectable by standard seismic networks (Elliott *et al.* 2016; Barbot *et al.* 2008). These are signals for which the satellite gravity acquisitions can give complementary information to space geodetic observations, especially for faults in oceanic areas for which surface deformation cannot be detected by interferometric Synthetic Aperture Radar acquisitions or by GNSS. These movements are though slow, extending over decades or centuries, and depending on the relative velocity of the moving plates across the fault discontinuity. Therefore, a monthly or yearly time resolution of the field can be already acceptable, if a lower magnitude can be detected by MAGIC. For this reason, in the case of solid Earth applications, it is useful to consider not only the weekly spectral error curve of MAGIC in recovering the HIS signal, but also the time-averaged error curves, which are subsequently lowered with increasing integration time interval, finally almost reaching the instrumental spectral noise curve. Given the error degree variance at SH degree l formulated for the solution time span Δt_0 (original time interval), variance $\sigma^2(l, \Delta t_0)$ and Δt_1 (time interval we are scaling to), variance $\sigma^2(l, \Delta t_1)$, the scaling law is the following:

$$\sigma^2(l, \Delta t_1) = \sigma^2(l, \Delta t_0) \frac{\Delta t_0}{\Delta t_1}. \quad (3)$$

The error curves are reduced by the approximate factor 2/100 in variance by extending the sampling from one week to one year, and, as will be shown later, lowering the curves, results in reduced minimum earthquake magnitude sensitivity for MAGIC. The earthquake is detectable if the signal spectrum in a given SH degree range is larger than the power of the degree error variance of MAGIC. Since the signal is local and not global, a spatial localization of the spectrum is required. We apply the spatio-spectral localization method in the SH domain proposed by Wieczorek *et al.* (2007), in its implementation in the SHTOOLS software (Wieczorek *et al.* 2018), and adopt the spherical cap as localization domain. If the localization operation is not applied, an observable earthquake spectrum results to be much lower and seemingly undetectable by the mission, which is not realistic when comparing the earthquake signal amplitude with the noise amplitude calculated on the Earth surface.

We compute the gravity field of an earthquake through the deformation in a radially layered spherical Earth model including coseismic and visco-elastic post-seismic deformation (software QSSP-STATIC, Wang *et al.* 2017). The layered Earth model consists of a purely elastic lithosphere in the first 40 km, overlying a Burgers model up to 120 km, then by two Maxwell bodies separated by an interface at 660 km. Properties from 1400 km to the Earth centre, are assumed constant.

The relevant parameters defining the earthquake source are the dip of the fault, the rake of slip and depth of fault. We have tested a multitude of combinations of the fault parameters, finding that the thrust fault maximizes the gravity signal. In the point-source approximation, for a given unit source-mechanism tensor, characterizing the earthquake mechanism, the tensor elements scale linearly

with the seismic moment. Therefore also the body forces which constitute the source term of the fault movement scale linearly with the seismic moment. Due to the harmonicity of the gravity field, this holds true for any derived functional and/or upward continued field. Therefore, the seismic moment is the controlling parameter of the amplitude of the gravity field. This allows to calculate the gravity field for one reference seismic moment, scaling the degree variances then for other seismic moments, without the need to recalculate the gravity field for the different fault plane solutions. In terms of degree variances of the gravity field, they scale with the square of the seismic moment. As seen in Fig. 14, a magnitude $M 8.2$ earthquake is at the limit of observation of the single polar pair after one year of data accumulation (GRACE-like scenario), the thrust event being seen only up to degree $N=45$, and is well above the detection limit for the Bender double pair, up to the maximum degree $N=65$ with the much higher time resolution of 1 week. This is comparable with the results of Chao & Liao (2012), who find that the earthquake signal is captured by GRACE down to $M 8.3$, by using an empirical orthogonal function (EOF) based strategy and a step-function model over a 2-yr time span: 1 yr before and 1 yr after the event, which can be consistently compared with the noise curves obtained with 1 yr of data accumulation. We also note that (de Viron *et al.* 2008) provided a 30 per cent detection for events of $M 8.1$ and 50 per cent for $M 8.8$ events in GRACE gravity solutions. Their strategy used post-processed monthly solutions and an EOF-based time-series analysis strategy that is expected to mitigate the effect of de-aliasing residuals. A direct comparison with our approach is therefore more difficult.

We calculate the cumulative RMS-per-degree spectra for the signal, for a number of significant simulated earthquakes, and error, in two selected scenarios (GRACE-like polar only and MAGIC Bender 3d.H). The cumulative RMS spectra at a given SH degree is representative of the signal and error RMS that can be observed in the spatial domain (i.e. by synthesizing the SH expansion on a discrete grid of computation points). We apply the aforementioned spatio-spectral localization in a 8° radius spherical cap, which results in a minimum SH degree of the localized spectra of $N=27$. These spectra are shown in Fig. 15, expressed in two functionals derived from the SH coefficients of the potential: EWH, using the conversion defined in eq. (1), and gravity, specifically the first radial derivative of the disturbing potential (T_r). The detection limits (the intersections of signal and error spectra) are invariant with respect to the employed functional. This serves as a control of consistent operations being carried out on the error and signal data. Signal is computed at a nominal ground level, equal by convention to the semimajor axis of WGS84. Note that the effect of a ground-tied measurement, which would be displaced by the surface displacement and be thus affected by the local gravity gradient, is removed from the modelled earthquakes signals reflecting the nature of a space-borne gravity measurement. The coseismic signal for a magnitude $M 8.0$ is about the limit for a weekly time resolution of MAGIC. Extending the resolution to 1 yr, the lower magnitude of $M 7.4$ could be observed. The worldwide detection of a $M 7.4$ and lower earthquake is done by seismological networks as well, but the information retrieved from gravity is the combined effect of aseismic afterslip and post-seismic relaxation, the modelling of which allows to further define the fault properties. In particular, the post-seismic relaxation can be predicted starting from the coseismic fault dislocation and making assumptions on the crust and mantle rheology, and therefore subtracted from the observed gravity signal to determine the fault afterslip. The limit of detection for a strike-slip mechanism requires a slightly greater

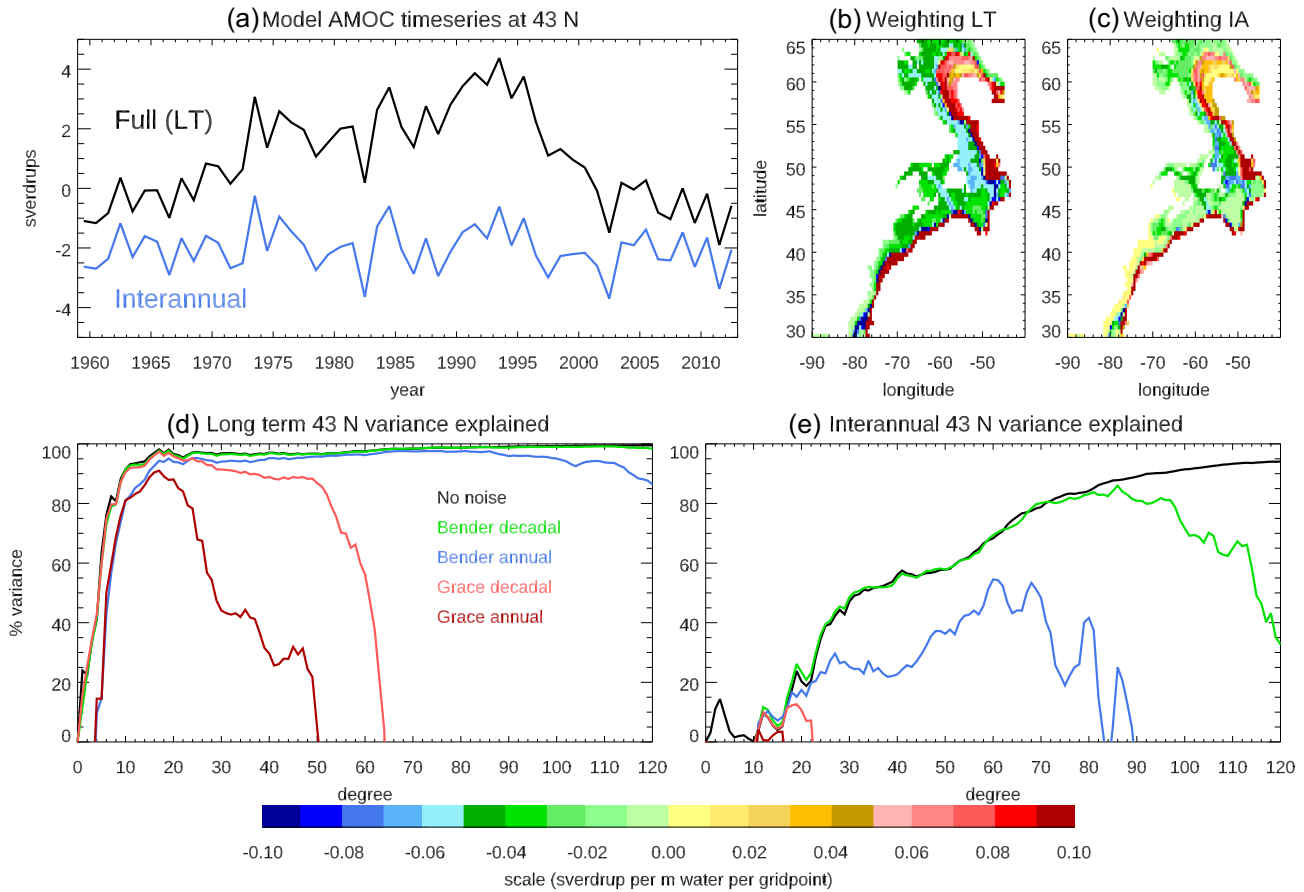


Figure 13. (a) Time-series of the Atlantic Overturning Circulation (overturning stream function at the depth of the maximum mean stream function) at 43° N (black), and after subtracting a running decadal mean (blue; the full time-series was extended with constant values at the ends to calculate this). (b) and (c) Weighting functions used to calculate the corresponding time-series from ocean bottom pressure. (d) and (e) Variance of the true weighted-average bottom pressure time-series explained by simulated observations, after truncating at different SH degrees, and under different observation scenarios. Weekly noise values were scaled by the square root of 52 (‘annual’) or 520 (‘decadal’) to approximate the noise at different timescales.

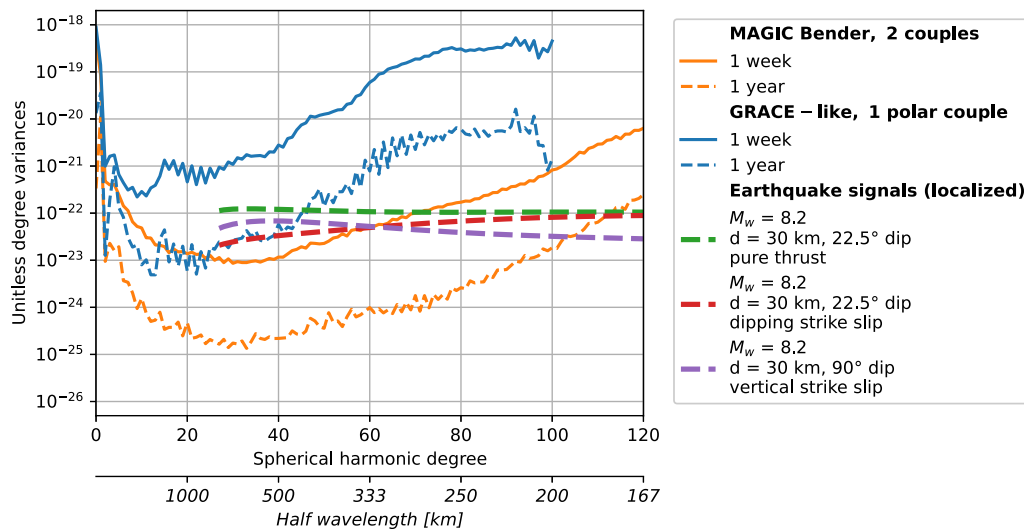


Figure 14. The localized spectrum of an M 8.2 magnitude earthquake. The MAGIC error curves are shown for 1 week and 1 yr time resolution. The earthquake spectra are shown for a pure thrust, and a dipping and vertical strike-slip fault. Earthquake depth is 30 km.

magnitude than the M 8.0 limit for the thrust event with weekly sampling. In summary, to analyse the performance of MAGIC in detecting a gravity signal generated by an earthquake of a limiting magnitude M , we simulate the gravity signal that is generated

by slip on a fault, given a seismic moment, to which a seismic magnitude is calculated. We define an earthquake to be observable if at least part of its spectral curve is above the spectral noise curve of the satellite mission. The seismic moment could be interpreted as

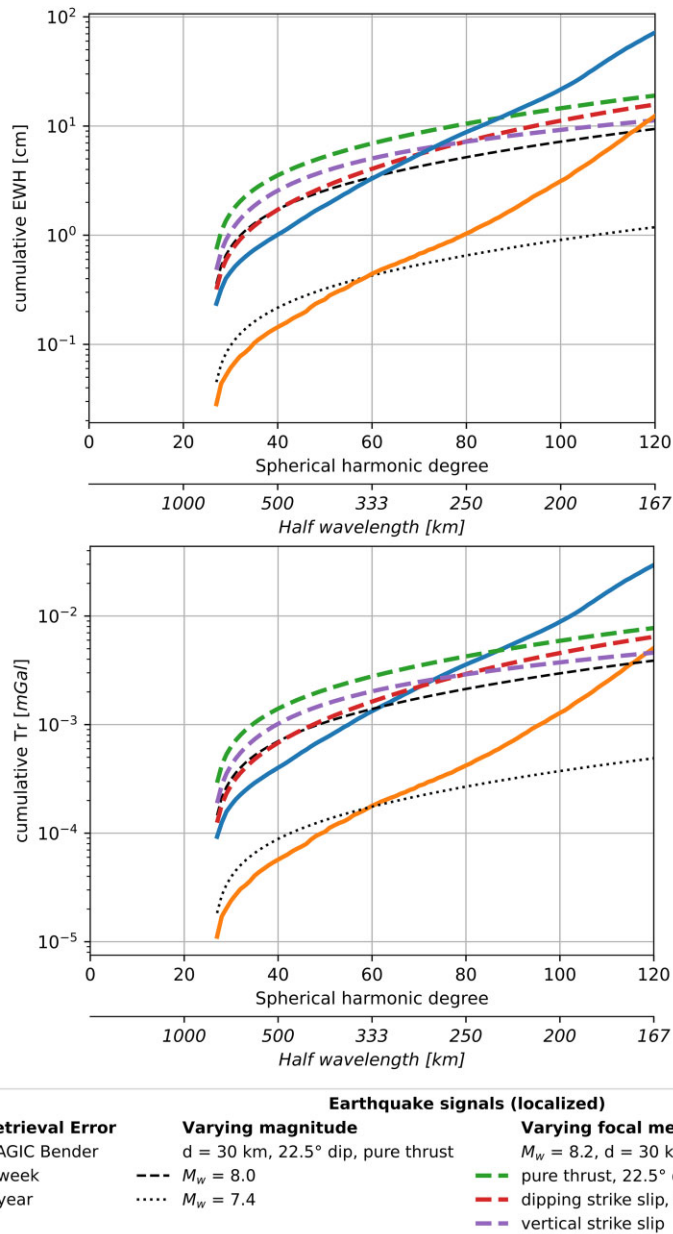


Figure 15. Spectral-domain comparison of the earthquake signals with retrieval errors in two selected scenarios (GRACE-like polar only and MAGIC Bender 3d_H). Top: EWH and bottom: first radial derivative of the disturbing potential (T_r). The spectra in both panels are expressed in RMS per SH degree, cumulative, at nominal ground level ($r = a_{WGSS4}$).

due to a coseismic signal, or due to a slow fault slip, and the gravity signal generated either in short time, or developing a trend distributed over time. The noise curve for a yearly time resolution has a degree variance that is smaller by a factor of 2/100 compared to a weekly time resolution, lowering the smallest observable seismic moment by the factor 0.14 (square root of 2/100), which translates into a moment magnitude reduction of 0.57 due to the difference in moment magnitude being $2/3 \cdot \log_{10}(0.14)$ (Wells & Coppersmith 1994). This is because the degree variance of the gravity signal scales with the square of the seismic moment. Comparing single- and double-pair configurations with weekly solutions shows that the double pair significantly lowers the detectable moment magnitude from M 8.8 to M 8.0, and increases the highest observable degree up to about 60 (333 km resolution). Given a certain earthquake

magnitude, the highest observable degree is defined by the SNR being equal to one or higher. The highest resolvable degree of the earthquake depends on its magnitude: fixing the requested spatial resolution of an earthquake to 333 km at weekly sampling, which corresponds to degree 60, the Bender configuration requires the magnitude to be M 8.0, whereas the GRACE-like configuration requires the magnitude to be M 9.2. Lowering the time resolution to 1 yr, the Bender configuration would detect earthquakes with magnitude M 7.4 upwards, at a spatial resolution of 333 km (degree 60). At higher degrees for this magnitude, the noise is expected to be larger than the earthquake signal. Undoubtedly, the MAGIC configuration will bring a definitive improvement compared to the present observation technology.

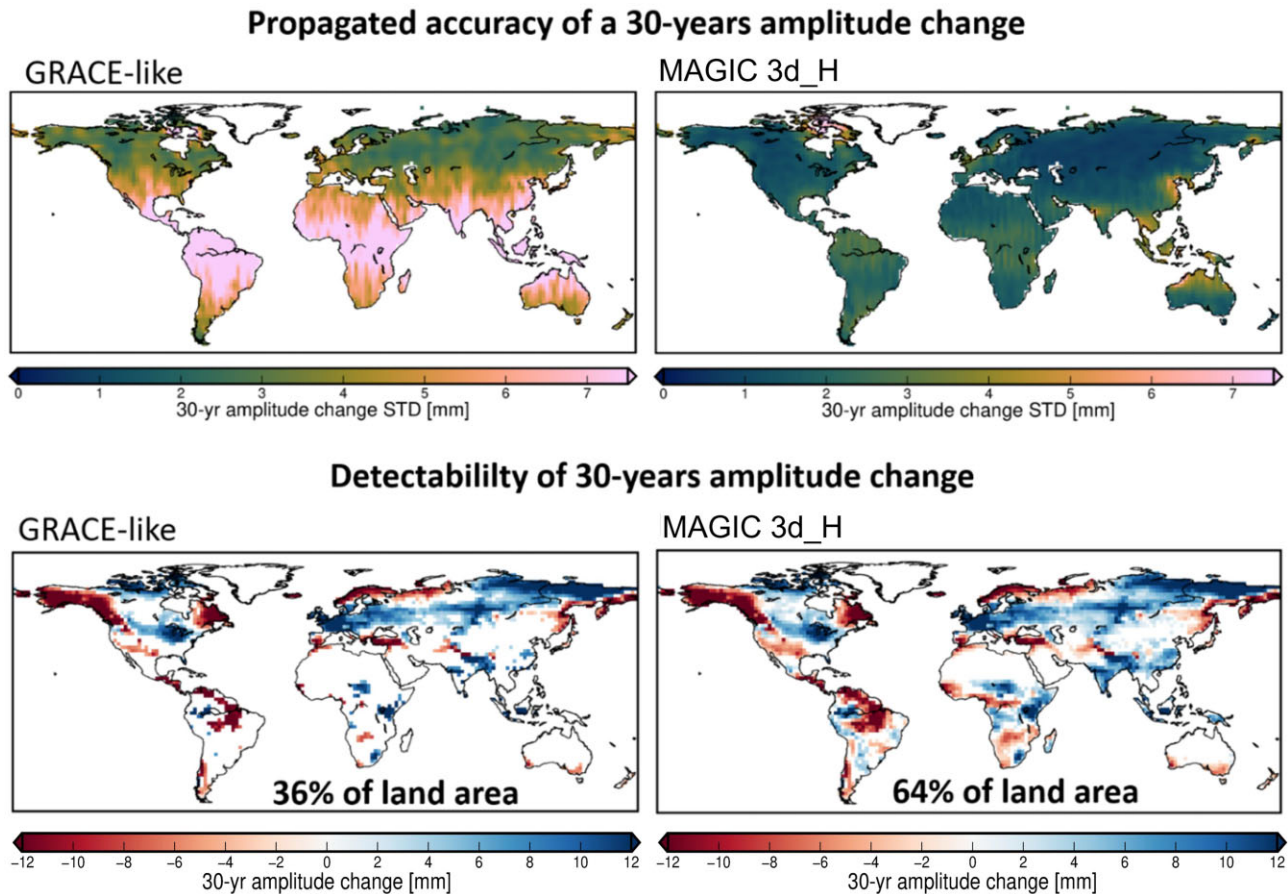


Figure 16. Top: standard deviation of GRACE-like (left) and MAGIC (right) TWS amplitude change of annual cycle over 30 yr. Bottom: detectability of amplitude change: coloured pixels denote where projected amplitude change exceeds the magnitude of the accuracy.

5.5 Climate change

Some theories suggest that climate change might lead to an ‘intensification’ of the global water cycle resulting in, for example, an increase in the annual amplitude of water storage change (Huntington 2006), and/or that climate-induced changes in atmospheric circulation patterns affect the phase of annual peaks (Dunning *et al.* 2018). Jensen *et al.* (2020) investigated the detectability of net TWS changes in the annual water cycle using satellite gravimetry. A satellite mission able to observe and quantify these changes would be beneficial in two ways: (i) satellite gravity could be used as tool to proof (or falsify) the postulate of an intensification of the water cycle in different regions of the world, and (2) the data could serve to validate whether climate models correctly simulate such changes. Jensen *et al.* (2020) computed projected changes in amplitude (fig. 7a of Jensen *et al.* 2020) and phase (fig. 8a of Jensen *et al.* 2020) derived from an ensemble of global climate models taking part in the CMIP6 model intercomparison project (Eyring *et al.* 2016).

To analyse the detectability of these projected changes of the annual cycle by current or future satellite gravimetry missions, they were compared to the achievable accuracies of these quantities from the GRACE-like and the MAGIC 3d_H simulation output following the methodology used in Jensen *et al.* (2020). To this end, the grid-wise RMSD values of the simulated 7-d temporal residuals were error propagated to derive standard deviations of amplitude/phase change after 30 yr. For the amplitude change, these standard deviations are shown in Fig. 16 (top) for the GRACE-like (left) and

for the MAGIC (right) scenarios. Here, VADER filtered solutions (Horvath *et al.* 2018) are used applying a relatively weak filter ($\alpha = 10$), as the unfiltered simulation output that was used in the above chapters is not suitable for the detection of these small changes. The projected amplitude changes (from Jensen *et al.* 2020) are now challenged against these uncertainties and coloured pixels in Fig. 16 (bottom) denote regions where the projected amplitude change exceeds the magnitude of the uncertainty. While, according to the simulations at hand, a GRACE-like scenario can only detect the anticipated amplitude changes in 36 per cent of the land area after 30 yr of observation, MAGIC-like scenario would be able to identify such changes in 64 per cent of the land area. Regarding changes in the annual phase, a detectability of a 30-yr phase change from the single-pair scenario can be identified in 30 per cent of the land area and a significant increase of this portion (56 per cent of land area) for the MAGIC scenario.

6 CONCLUSIONS AND RECOMMENDATIONS

The investigations presented in this paper have demonstrated the superior performance of Bender double-pair in-line mission concepts over other potential constellation architectures, such as single-pair in-line, SSO, or pendulum. As for all gravity missions, the altitude remains the main performance driver. In case of MAGIC, a low altitude together with a high-performance instrumentation of the inclined pair was shown to be crucial in satisfying the user needs. The

comparison of the cumulative errors with the IUGG user requirements once again confirmed that to meet threshold requirements and approach target requirements, a Bender double-pair mission is required. The reduced uncertainty offered by the MAGIC constellation allows for a wide use of 7-d Level-2 time-varying gravity products even with less need of post-processing by means of filtering.

An intercomparison of MAGIC and GRACE-type scenarios was performed by means of Level-2 synthetic products, consistent with the approach on answering user requirements and forward-looking to a future mass-change product with less need of post-processing. The analyses of MAGIC scenarios for different application areas in the field of geosciences confirmed that the double-pair configuration will significantly enlarge the number of observable mass-change phenomena by resolving smaller spatial scales with sufficient accuracy. In this way, also hitherto indiscernible Earth system processes can be unravelled and quantified with the MAGIC constellation.

For hydrological applications, the MAGIC constellation will provide a significant added value because the number of hydrological units such as river basins or aquifers that can be analysed for water storage variations with certain accuracy requirements will markedly increase compared to a GRACE-like mission. For unfiltered solutions, the threshold accuracy of 10.1 cm EWH given in the current MRD at high spatial resolution (260 km) can be fulfilled by the analysed double-pair scenarios for more than 90 per cent of the river basins worldwide, whereas at the lower spatial resolution of 400 km, the MRD threshold accuracy may need to be relaxed to 2.5 or 3.5 cm EWH to resolve TWS variations in 67 and 90 per cent of the investigated river basins, respectively.

The proposed MAGIC double-pair configurations will significantly improve our ability to monitor mass displacements on the ice sheets compared to what is currently possible. For example, our results show that it should become feasible to separate mass-change signals in the interior of GrIS from those in the coastal zones, and resolve small-scale mass variations in challenging regions such as the AIS Peninsula. The 5d_Mb configuration shows the best performance for the cryosphere applications evaluated here, with the largest number of regions of GrIS and AIS passing the threshold and target criteria of the current MRD.

For oceanography, the obtained results also confirmed that the MAGIC double-pair configurations produce a great improvement in ocean bottom pressure determination over a single pair GRACE-like configuration. By extending to SH degrees that permit clear physical interpretation up to between degree 50 and about 80, depending on the signal, there is the potential to monitor MOC changes on timescales of years and decades. For the Caribbean Sea example analysed here, it is shown that hitherto barely detectable signals of about 1 cm EWH RMS variability become detectable and with optimization of methods, the MAGIC configuration is expected to be able to explain 80–90 per cent of its variance.

Comparing weekly solutions for single- and double-pair configurations, it was shown that MAGIC will significantly lower the detectable earthquake moment magnitude from M 8.8 to M 8.0, and increase the highest observable degree up to about 60 (333 km resolution). Lowering the time resolution to 1 yr, the Bender constellation would be able to detect earthquakes with magnitude M 7.4 upwards, at the same spatial resolution of 333 km.

Under the climate change thematic field, a GRACE-like mission can only detect the anticipated amplitude changes in 36 per cent of the land area after 30 yr of observation. MAGIC turned out to be able to identify such changes in 64 per cent of the land area. For changes in the annual phase, a detectability of a 30-yr phase change from the

single-pair scenario can be again identified in only 30 per cent of the land area, while MAGIC enables a detectability over 56 per cent of land area.

These promising results in various applications fields demonstrate, that MAGIC will have great potential to lift mass transport monitoring from space to a next level. As already mentioned in Introduction, one of the main goals of MAGIC will be to provide also short-term (fast-track) products with short latency for operational service applications, such as drought and flood monitoring and prediction, and water management. The expected impact of MAGIC in this domain is currently being investigated and quantified, and related impact studies will be part of future work.

ACKNOWLEDGMENTS

This main work presented in this paper was performed in the framework of the project ‘NGGM/MAGIC—SCIENCE SUPPORT STUDY DURING PHASE A’, ESA-ESTEC, Contract 4000134613/21/NL/FF/ab funded by the European Space Agency. The authors would like to thank the members of the consortium study for their contribution.

DATA AVAILABILITY

The Level-2 gravity field simulated data used in this publication are freely available on the International Centre for Global Earth Models (ICGEM) website: <http://icgem.gfz-potsdam.de/sl/simulated>, and shall be cited as Daras *et al.* (2023). The reports and simulations’ results of the acknowledged project are freely available on the following website: <https://www.asg.ed.tum.de/en/iapg/magic/>.

REFERENCES

- Abyrkosov, P., Sulzbach, R., Pail, R., Dobsław, H. & Thomas, M., 2021. Treatment of ocean tide background model errors in the context of GRACE/GRACE-FO data processing, *Geophys. J. Int.*, **228**(3), 1850–1865.
- Abyrkosov, P., Murböck, M., Hauk, M., Pail, R. & Flechtner, F., 2022. Data-driven multi-step self-de-aliasing approach for GRACE and GRACE-FO data processing, *Geophys. J. Int.*, **232**(2), 1006–1030.
- Barbot, S., Hamiel, Y. & Fialko, Y., 2008. Space geodetic investigation of the coseismic and postseismic deformation due to the 2003 Mw 7.2 Altai earthquake: Implications for the local lithospheric rheology, *J. geophys. Res.*, **113**, B03403, doi:10.1029/2007JB005063.
- Bender, P., Wiese, D. & Nerem, R., 2008. A possible dual-grace mission with 90 degree and 63 degree inclination orbits, in *Proceedings of the 3rd International Symposium on Formation Flying, Missions and Technologies*, pp. 1–6, ESA/ESTEC, Noordwijk, The Netherlands.
- Cazenave, A. *et al.*, 2019. Observational requirements for long-term monitoring of the global mean sea level and its components over the Altimetry Era, *Front. Mar. Sci.*, **6**, 582, doi:10.3389/fmars.2019.00582.
- Ciraci, E., Velicogna, I. & Swenson, S., 2020. Continuity of the mass loss of the world’s glaciers and ice caps from the GRACE and GRACE Follow-On missions, *Geophys. Res. Lett.*, **47**, e2019GL086926, doi:10.1029/2019GL086926.
- Croteau, M.J., Nerem, R.S., Loomis, B.D. & Sabaka, T.J., 2020. Development of a daily GRACE mascon solution for terrestrial water storage, *J. geophys. Res.: Solid Earth*, **125**(3), doi:10.1029/2019jb018468.
- Chao, B.F. & Liau, J.R., 2019. Gravity changes due to large earthquakes detected in GRACE satellite data via empirical orthogonal function analysis, *J. geophys. Res.: Solid Earth*, **124**, 3024–3035.

- Daras, I., Pail, R., Murböck, M. & Yi, W., 2015. Gravity field processing with enhanced numerical precision for LL-SST missions, *J. Geod.*, **89**(2), 99–110.
- Daras, I., 2016. Gravity field processing towards future LL-SST satellite missions, *Deutsche Geodätische Kommission der Bayerischen Akademie der Wissenschaften*, ed. ,Reihe, C., pp. 23–39, Dissertationen, Heft.
- Decadal Survey, 2017. *Thriving on our Changing Planet—Decadal Survey for Earth Science and Applications from Space*, The National Academies of Sciences, Engineering, Medicine , doi:10.17226/24938.
- de Viron, O., Panet, I., Mikhailov, V., Van Camp, M. & Diament, M., 2008. Retrieving earthquake signature in grace gravity solutions, *Geophys. J. Int.*, **174**(1), 14–20.
- Daras, I. et al., 2023. Level-2a simulated gravity field solutions of ESA's science support study to Mass change And Geosciences International Constellation (MAGIC) Phase A., V. 1.0, *GFZ Data Serv.* , doi:10.5880/icgem.2023.005.
- Delman, A. & Landerer, F., 2022. Downscaling satellite-based estimates of ocean bottom pressure for tracking deep ocean mass transport, *Remote Sens.*, **14**, 1764 , doi:10.3390/rs14071764.
- Dobslaw, H., Bergmann-Wolf, I., Dill, R., Forootan, E., Klemann, V., Kusche, J. & Sasgen, I., 2015. The updated ESA Earth System Model for future gravity mission simulation studies, *J. Geod.*, **89**(5), 505–513.
- Dobslaw, H., Bergmann-Wolf, I., Forootan, E., Dahle, C., Mayer-Gürr, T., Kusche, J. & Flechtner, F., 2016. Modeling of present-day atmosphere and ocean non-tidal de-aliasing errors for future gravity mission simulations, *J. Geod.*, **90**(5), 423–436.
- Drinkwater, M.R., Floberghagen, R., Haagmans, R., Muzi, D. & Popescu, A., 2003. GOCE:ESA's first Earth Explorer Core mission, *Earth Gravity Field from Space – From Sensors to Earth Sciences, Space Sciences Series of ISSI*, Vol. 17, pp. 419–432, eds ,Beutler, G., ,Drinkwater, M.R., ,Rummel, R.& & ,von Steiger, R., Kluwer Academic Publishers, Dordrecht, The Netherlands.
- Dunning, C.M., Black, E. & Allan, R.P., 2018. Later wet seasons with more intense rainfall over Africa under future climate change, *J. Clim.*, **31**, 9719–9738.
- Elliott, J., Walters, R. & Wright, T., 2016. The role of space-based observation in understanding and responding to active tectonics and earthquakes, *Nat. Commun.*, **7**, 13844 , doi:10.1038/ncomms13844.
- Elsaka, B., et al., 2013. Comparing seven candidate mission configurations for temporal gravity field retrieval through full-scale numerical simulation, *J. Geod.*, **88**, 31–43.
- Eyring, V., Bony, S., Meehl, G.A., Senior, C.A., Stevens, B., Stouffer, R.J. & Taylor, K.E., 2016. Overview of the Coupled Model Intercomparison Project Phase 6 (CMIP6) experimental design and organization, *Geosci. Model Develop.*, **9**(5), 1937–1958.
- & Thomas, G., 2006. Evidence for intensification of the global water cycle: Review and synthesis, *J. Hydrol.*, **319**(1), 83–95.
- Landerer, F.W. et al., 2020. Extending the Global Mass Change Data Record: GRACE Follow-On instrument and science data performance, *Geophys. Res. Lett.*, **47**(12) , doi:10.1029/2020GL088306.
- Elipot, S., Frajka-Williams, E., Hughes, C.W. & Willis, J., 2014. The observed North Atlantic Meridional Overturning Circulation: its meridional coherence and ocean bottom pressure, *J. Phys. Oceanogr.*, **44**(2), 517–537.
- Fettweis, X. et al., 2020. GrSMBMIP: intercomparison of the modelled 1980–2012 surface mass balance over the Greenland Ice Sheet, *Cryosphere*, **14**, 3935–3958.
- GRDC, 2020. *Major River Basins of the World/Global Runoff Data Centre, GRDC. 2nd, rev. ext. ed.*, Federal Institute of Hydrology (BfG), Koblenz, Germany.
- Haagmans, R. & Tsaoussi, L., 2020. *Next Generation Gravity Mission as a Mass-change And Geosciences International Constellation (MAGIC) Mission Requirements Document*, Earth and Mission Science Division, European Space Agency; NASA Earth Science Division , doi:10.5270/esa.nasa.magic-mrd.2020.
- Hauk, M. & Wiese, D.N., 2020. New methods for linking science objectives to remote sensing observations: a concept study using single and dual-pair satellite gravimetry architectures, *Earth Space Sci.*, **7**(3) , doi:10.1029/2019EA000922.
- Heller-Kaikov, B., Pail, R. & Daras, I., 2023. Mission design and processing aspects for the Mass Change and Geoscience International Constellation (MAGIC). , *Geophysical Journal International*, **235**(1), 718–735. doi:10.1093/gji/ggad266.
- Horvath, A., Murböck, M., Pail, R. & Horvath, M., 2018. Decorrelation of GRACE time variable gravity field solutions using full covariance information, *Geosciences*, **8**(9), 323. doi:10.3390/geosciences8090323.
- Hughes, C.W., Williams, J., Hibbert, A., Boening, C. & Oram, J., 2016. A Rossby whistle: a resonant basin mode observed in the Caribbean Sea, *Geophys. Res. Lett.*, **43**, 7036–7043.
- Hughes, C.W., Williams, J., Blaker, A., Coward, A. & Stepanov, V., 2018. A window on the deep ocean: the special value of ocean bottom pressure for monitoring the large-scale, deep-ocean circulation, *Prog. Oceanogr.*, **161**, 19–46.
- IMBIE team, 2018. Mass balance of the Antarctic Ice Sheet from 1992 to 2017, *Nature*, **558**(7709), 219–222.
- IMBIE team, 2020. Mass balance of the Greenland Ice Sheet from 1992 to 2018, *Nature*, **579**(7798), 223–239.
- Iran Pour, S. et al., 2015. *Assessment of satellite constellations for monitoring the variations in Earth gravity field (SC4MGV)*, Final Report, ESA/ESTEC Contract No. AO/1-7317/12/NL/AF.
- International Union for Geodesy and Geophysics (IUGG) (Ed.), 2015. IUGG Resolutions at the XXVI General Assembly: 22 June - 2 July 2015; Prague, Czech Republic., Resolution 2: Future Satellite Gravity and Magnetic Mission Constellations, *XXVI General Assembly of the International Union of Geodesy and Geophysics (IUGG) (Prague 2015)*, Karlsruhe : IUGG Secretariat, KIT Karlsruhe Institute of Technology, https://gfzpublic.gfz-potsdam.de/rest/items/item_1626895_1/component/file_1626894/content, accessed on 05/01/2024.
- International Union for Geodesy and Geophysics (IUGG) (Ed.), 2023. IUGG Resolutions at the XXVIII General Assembly: 11 July - 20 July 2023; Berlin, Germany, Resolution 2: Sustained Terrestrial Water Storage (TWS) Monitoring by Dedicated Gravity Satellite Constellations, *XXVIII General Assembly of the International Union of Geodesy and Geophysics (IUGG) (Berlin 2023)*, https://iugg.org/wp-content/uploads/2023/09/2023_IUGG-GA-Resolutions.pdf, accessed on 05/01/2024.
- Jensen, L., Eicker, A., Dobslaw, H. & Pail, R., 2020. Emerging changes in Terrestrial Water Storage variability as a target for future satellite gravity missions, *Remote Sens.*, **12**(23), 3898 , doi:10.3390/rs12233898.
- Massotti, L., Siemes, C., March, G., Haagmans, R. & Silvestrin, P., 2021. *Next Generation Gravity Mission Elements of the Mass Change and Geoscience International Constellation: from orbit selection to instrument and mission design* , doi:10.3390/rs13193935.
- Massotti, L. et al., 2022. *Next Generation Gravity Mission Design Activities within the Mass Change and Geoscience International Constellation*, SPIE Remote Sensing (RS103), Berlin, Germany.
- Mayer-Gürr, T. et al., 2015. The combined satellite gravity field model GOCO05s, *Geophys. Res. Abstr.*, **17**, EGU2015–12364. European Geosciences Union General Assembly 2015 (Vienna, Austria), doi:10.13140/RG.2.1.4688.6807.
- McCarthy, G.D. et al., 2020. Sustainable observations of the AMOC: methodology and technology, *Rev. Geophys.*, **58**(1), e2019RG000654 , doi:10.1029/2019RG000654.
- Noël, B., van de Berg, W.J., Lhermitte, S. & van den Broeke, M.R., 2019. Rapid ablation zone expansion amplifies north Greenland mass loss, *Sci. Adv.*, **5**, eaaw0123 , doi:10.1126/sciadv.aaw0123.
- Pail, R. et al., 2015. *Observing Mass Transport to Understand Global Change and to Benefit Society: Science and User Needs – An international multi-disciplinary initiative for IUGG*, Deutsche Geodätische Kommission der Bayerischen Akademie der Wissenschaften, Heft 320, München , https://gfzpublic.gfz-potsdam.de/pubman/item/item_1354175.
- Pail, R. et al., 2019. *Additional Constellation & Scientific Analysis of the Next Generation Gravity Mission Concept (ADDCON)*, Final Report, ESA/ESTEC Contract No. 4000118480/16/NL/FF/gp.
- Pail, R. et al., 2022. *NGGM/MAGIC – Science Support Study During Phase A*, Final Report, ESA/ESTEC Contract No. RFP/3-17035/20/NL/FF/tdf. <https://www.asg.ed.tum.de/iapg/magic/documents/>.

- Purkhauser, A.F., Siemes, C. & Pail, R., 2020. Consistent quantification of the impact of key mission design parameters on the performance of next-generation gravity missions, *Geophys. J. Int.*, **221**, 1190–1210.
- Ran, J. *et al.*, 2018. Seasonal mass variations show timing and magnitude of meltwater storage in the Greenland Ice Sheet, *Cryosphere*, **12**, 2981–2999.
- Ray, R., 2008. *GOT4.7. Extension of Ray R (1999) A global ocean tide model from Topex/Poseidon altimetry GOT99.2*, NASA Tech Memo 209478.
- Reigber, C. *et al.*, 2002. A high quality global gravity field model from CHAMP GPS tracking data and accelerometry (EIGEN-1S), *Geophys. Res. Lett.*, **29**, 14, doi:10.1029/2002GL015064.
- Rodell, M., Famiglietti, J.S., Wiese, D.N., Reager, J.T., Beaulieu, H.K., Landerer, F.W. & Lo, M.-H., 2018. Emerging trends in global freshwater availability, *Nature*, **557**, 651–659.
- Sasgen, I. *et al.*, 2012. Timing and origin of recent regional ice-mass loss in Greenland, *Earth planet. Sci. Lett.*, **333–334**, 293–303.
- Savcenko, R. & Bosch, W., 2012. *EOT11a—empirical ocean tide model from multi-mission satellite altimetry*, DGF-Report No.89.
- Schlegel, N.-J., Wiese, D.N., Larour, E.Y., Watkins, M.M., Box, J.E., Fettweis, X. & van den Broeke, M.R., 2016. Application of GRACE to the assessment of model-based estimates of monthly Greenland Ice Sheet mass balance (2003–2012), *Cryosphere*, **10**, 1965–1989.
- Tapley, B.D., Bettadpur, S., Watkins, M. & Reigber, C., 2004. The gravity recovery and climate experiment experiment: mission overview and early results, *Geophys. Res. Lett.*, **31**(9), doi:10.1029/2004gl019920.
- Thomas, B., Famiglietti, J., Landerer, F., Wiese, D., Molotch, N. & Argus, D., 2017. GRACE Groundwater Drought Index: evaluation of California Central Valley groundwater drought, *Remote Sens. Environ.*, **198**, 384–392.
- Visser, P. *et al.*, 2016. *Towards a Sustained Observing System for Mass Transport to Understand Global Change and to Benefit Society*, NASA/ESA Interagency Gravity Science Working Group (IGSWG), Doc. nr.: TUDIGSWG-2016-01.
- Wahr, J., Molenaar, M. & Bryan, F., 1998. Time variability of the Earth's gravity field: hydrological and oceanic effects and their possible detection using GRACE, *J. geophys. Res. (Solid Earth)*, **103**(B12), 30205–30229.
- Wang, R., Heimann, S., Zhang, Y., Wang, H. & Dahm, T., 2017. Complete synthetic seismograms based on a spherical self-gravitating Earth model with an atmosphere–ocean–mantle–core structure, *Geophys. J. Int.*, **210**, 1739–1764.
- Wells, D.L. & Coppersmith, K.J., 1994. New empirical relationships among magnitude, rupture length, rupture width, rupture area, and surface displacement, *Bull. seism. Soc. Am.*, **84**, 974–1002.
- Wieczorek, M.A. & Simons, F.J., 2007. Minimum-variance multitaper spectral estimation on the sphere, *J. Fourier Anal. Appl.*, **13**, 665–692.
- Wieczorek, M.A. & Meschede, M., 2018. SHTools: tools for working with spherical harmonics, *Geochem. Geophys. Geosyst.*, **19**, 2574–2592.
- Wiese, D.N. *et al.*, 2022. The mass change designated observable study: overview and results, *Earth Space Sci.*, **9**(8), doi:10.1029/2022EA002311.
- Wouters, B., Chambers, D. & Schrama, E.J.O., 2008. GRACE observes small-scale mass loss in Greenland, *Geophys. Res. Lett.*, **35**(20), doi:10.1029/2008GL034816.
- Wouters, B., Gardner, A.S. & Moholdt, G., 2019. Global Glacier mass loss during the GRACE Satellite Mission (2002–2016), *Front. Earth Sci.*, **7**(96), doi:10.3389/feart.2019.00096.
- Zwally, H.J., Giovinetto, M.B., Beckley, M.A. & Saba, J.L., 2012. *Antarctic and Greenland Drainage Systems*, GSFC Cryospheric Sciences Laboratory, http://icesat4.gsfc.nasa.gov/cryo_data/ant_grn_drainage_systems.php, accessed on 05/01/2024.
- Zhou, H., Luo, Z., Zhou, Z., Yang, F., Pail, R., Tu, L., Yeh, H.-C. & Yang, S., 2021. What can we expect from the inclined satellite formation for temporal gravity field determination?, *Surv. Geophys.*, **42**(3), 699–726, Springer Science and Business Media LLC, doi:10.1007/s10712-021-09641-9.

APPENDIX A: MAGIC ORBIT SCENARIOS

Orbits sets for inclined (IP or P2) and polar (PP or P1) pairs. The ID shows the number of subcycle days for which the set is optimized and an additional information about the altitudes: (M)id, (H)igh.

Note that the semimajor axis is reduced by 6378 km for highlighting differences in altitude. The other columns provide information about the homogeneity, longitude shift and sub-cycles of the ground-track patterns; more details are described in Massotti *et al.* (2021) and Haagmans & Tsaoussi (2020).

Table A1. Orbit design parameters of constellation sets including inclined (IP or P2) and polar (PP or P1) pairs.

ID	IP Alt. [km]	IP Inc. [°]	PP Alt. [km]	PP Inc. [°]	hl IP [-]	hl PP [-]	Lon. shift IP [°]	Lon. shift PP [°]	Subcycles [d]
3d_M	409	70	440	89	1.368	1.383	2.308	2.384	2, 3, 8, 11, 30
3d_H	432	70	463	89	1.451	1.449	-3.076	-3.067	3, 7, 31
5d_Ma	396	65	434	89	1.397	1.383	-1.499	-1.458	2, 3, 5, 13, 18, 31
5d_Mb	397	70	425	87	1.168	1.167	0.736	0.733	2, 5, 27, 32
5d_H	465	75	488	89	1.185	1.190	0.762	0.781	4, 5, 29
7d_M	389	70	417	87	1.238	1.253	0.743	0.786	2, 7, 30
7d_H	432	70	463	89	1.218	1.226	0.672	0.692	3, 7, 31
SSO for 3d_H	477	97	463	89	1.454	1.449	-3.097	-3.067	3, 7, 31
SSO for 7d_H	477	97	463	89	1.201	1.226	0.622	0.692	3, 7, 31
5d_LL	344	70	376	89	1.423	1.410	-1.671	-1.628	1, 2, 5, 12, 29
5d_LH	344	71.5	492	89	1.169	1.172	-0.732	-0.790	5, (32-31)
U3d5d_H	432	70	492	89	1.451 (3d)	1.172 (5d)	-3.076 (3d)	-0.790 (5d)	IP: 3, 31; PP: 5, 31
U5d_H	460	70	492	89	1.061 (5d)	1.172 (5d)	-0.284 (5d)	-0.790 (5d)	IP: 5; PP: 5, 31
U3d_H	402	65	463	89	1.382	1.449	2.380	-3.067	IP: 3, 29-30; PP: 3, 7, 31